Reaction and diffusion at the reservoir/ shale interface during CO_2 storage: impact of geochemical kinetics

Victor N. Balashov[1*], George D. Guthrie[2], Christina L. Lopano[3], J. Alexandra Hakala[3], Susan L. Brantley[1]

[1]Earth and Environmental Systems Institute, 2217 EES Building, Pennsylvania State University, University Park, PA 16802; [2] Los Alamos National Laboratory, Mail Stop D446, Los Alamos, NM 87545; [3] U.S. Department of Energy, National Energy and Technology Laboratory, 626 Cochrans Mill Road, Pittsburgh, PA 15236

Abstract

We use a reactive diffusion model to investigate what happens to CO_2 injected into a subsurface sandstone reservoir capped by a chlorite- and illite-containing shale seal. The calculations simulate reaction and transport of supercritical (SC) CO_2 at 348.15 K and 30 MPa up to 20,000 a. Given the low shale porosity (5%), chemical reactions mostly occurred in the sandstone for the first 2000 a with some precipitation at the ss/sh interface. From 2000 to 4000 a, ankerite, dolomite and illite began replacing Mg-Fe chlorite at the sandstone /shale interface. Transformation of chlorite to ankerite is the dominant reaction occluding the shale porosity in most simulations: from 4000 to 7500 a, this carbonation seals the reservoir and terminates reaction. Overall, the carbonates (calcite, ankerite, dolomite), chlorite and goethite all remain close to local chemical equilibrium with brine. Quartz is almost inert from the point of its dissolution/precipitation. However, the rate of quartz reaction controls the long-term decline in aqueous silica activity and its evolution toward equilibrium. The reactions of feldspars and clays depend strongly on their reaction rate constants (microcline is closer to local equilibrium than albite). The timing of porosity occlusion mostly therefore depends on the kinetic constants of kaolinite and illite. For example, an increase in the kaolinite kinetic constant by 0.25 logarithmic units hastened porosity closure by 4300 a. The earliest simulated closure of porosity occurred at approximately 108 a for simulations designed as sensitivity tests for the rate constants.

These simulations also emphasize that the rate of CO_2 immobilization as aqueous bicarbonate (solubility trapping) or as carbonate minerals (mineral trapping) in sandstone reservoirs depends upon reaction kinetics -- but the relative fraction of each trapped CO_2 species only depends upon the initial chemical composition of the host sandstone. For example, at the point of porosity occlusion the fraction of bicarbonate remaining in solution depends upon the initial Na and K content in the host rock but the fraction of carbonate mineralization depends only on the Ca, Mg, Fe content. Since ankerite is the dominant mineral that occludes porosity, the dissolved concentration of ferrous iron is also an important parameter. Future efforts should focus on cross-comparisons and ground-truthing of simulations made for standard case studies as well as laboratory measurements of the reactivities of clay minerals.

1. Introduction

Climate change is impacting human systems on Earth as the concentration of greenhouse gas CO_2 increases in the atmosphere. A potential solution to mitigate increases in atmospheric CO_2 is to capture CO_2 and inject it into deep rock formations such as sandstone reservoirs capped by

* Corresponding author. E-mail address: vnb1@psu.edu (V.N. Balashov).

shale. To understand such subsurface geologic sequestration of CO_2, we previously reported a case study consisting of a baseline sandstone reservoir + brine in the 8-component system SiO_2 – Al_2O_3 – CaO – Na_2O – K_2O – HCl – CO_2 – H_2O (Balashov et al., 2013). We presented a model where CO_2-enriched fluid was injected into a brine-filled sandstone bounded on the top and bottom by low-permeability shale. In the previous paper, only reactions in the sandstone were simulated in a one-dimensional problem with diffusion as the only transport mechanism. By 4000 a, the system had evolved toward a state where 97% (34.5 kg per m^3 of sandstone) of the maximum sequestration of CO_2 (dissolved + mineral-trapped CO_2) was attained.

Our first simulation showed that most of the reaction took place at pH 5.5-6.0. Although chemical equilibrium was not achieved until 25,000 a, after 4000 a, no more CO_2 redistributed from the supercritical phase. At 4000 a, about 20% of the sequestered CO_2 was dissolved as molecular $CO_{2(aq)}$, 50% was dissolved as HCO_3^-, and 30% had been precipitated as calcite. Thus solubility trapping (70%) dominated over mineral trapping (30%). We showed that a very useful first-order, *a priori* estimate of the extent of sequestration of the CO_2 as HCO_3^- could be simply determined as the amount of sodium in primary minerals in the sandstone (i.e., oligoclase); likewise, the extent of trapping as calcite could be determined *a priori* by the initial content of Ca in silicates (e.g. oligoclase+smectite).

Such reactive transport simulations remain to be ground-truthed. However recently, CO_2 trapping at Bravo Dome (New Mexico) – perhaps the largest known natural trap of CO_2 -- was analyzed (Sathaye et al., 2014) (Gilfillan et al., 2009) and we can compare it here to our previous computations. Like our estimates, most of the CO_2 gas is sequestered at Bravo Dome as dissolved molecular CO_2 present at a pH between 6 and 7, with a moderate amount of aqueous HCO_3^-. The occurrence of corroded feldspars in Bravo Dome Tubb sandstones are also consistent with our model: like our modelling, plagioclase showed the greatest corrosion as compared to K-feldspar (Baines and Worden, 2004; Pearce et al., 1996). An isotopic analysis (Gilfillan et al., 2009) is also consistent with up to 18% of the sequestered CO_2 present as mineral precipitate. This fraction is within a factor of 2 of our estimate of 30% for baseline sandstone composition.

In our previous modeling (BALASHOV et al., 2013), the reaction kinetics of albite and kaolinite played important roles in governing timing. The time period (~ 4000 a) predicted by the model for intensive reaction kinetics coincided with the time when supercritical (SC) CO_2 was redistributing into the brine by dissolution and carbonate precipitation. The rest of the equilibration time (~20,000 a) was characterized by the reaction of microcline (Mc) + kaolinite (Kln) $\rightarrow$ illite (Ill) + quartz (Qtz). A sensitivity analysis of the kinetic constants for oligoclase, albite and smectite demonstrated that timing of the equilibration of SC CO_2 in the sandstone system depended on these constants because they controlled the concentrations of aqueous Ca and Na, which in turn controlled the extent of calcite precipitation and formation of bicarbonate respectively.

Models of mineral/fluid reaction and transport are sensitive to many sources of uncertainty. First, there are experimental errors. Second, differences are often observed between reaction rates measured at the laboratory and field scales (White and Brantley, 2003). Often reactions in porous rock proceed closer to equilibrium than reactions in the laboratory (Arvidson and Lüttge, 2010). The next source of uncertainty is in upscaling from the pore-grain scale to the level of the

representative elemental volume (REV) of the rock (Kang et al., 2010; Li et al., 2007). Uncertainty is also entailed in describing the reactive surface area of minerals – in other words, not all sites on a surface are equally reactive (GAUTIER et al., 2001; RIMSTIDT et al., 2012; WASHTON et al., 2008). Therefore, sensitivity tests must be run to understand how uncertainties in kinetic data, in mechanisms, in upscaling and in mineral active surface area affect model output.

Here we apply the approach we developed earlier (Balashov et al., 2013) to probe the impact of uncertainties. We use a simple general kinetic law for mineral/ fluid interaction to explore the uncertainties by systematically varying kinetic constants by ± 1 order of magnitude. The uncertainties inherent in modelling transport are also evaluated by varying the Archie formation factor.

Our current model is still one-dimensional, but we have extended our earlier model by incorporating the shale caprock. This required addition of four new chemical components to the system (MgO, FeO, O_2, H_2SO_4). This model allows us to simulate diffusive alteration at the interface of the sandstone/shale (ss/sh). Diffusion is the main transport process at the caprock interface because of the low porosity and high tortuosity of the shale. With our model we seek to understand how the shale interacts with CO_2 during sequestration.

2. Geophysical and Geochemical Conditions

Mineral reactivity is strongly influenced by temperature, which affects solubility and reaction kinetics, and by the confining pressure, which determines the maximum CO_2 pressure attainable. Constraints on temperature (T) and pressure (P) for the baseline sandstone reservoir were described in our first paper where we investigated a system at 2 km depth (Balashov et al., 2013). Temperature, T was set at 75°C and pressure, P, at 30 MPa.

Table 1. Average composition of North American oil field brines based on published compositions (Collins, 1975).

Species	mg/L	molality	N
Cl^-	74800	2.1071	3397
Na^+	37260	1.6201	3397
Ca^{2+}	7860	0.1960	3392
Mg^{2+}	1510	0.0623	3364
SO_4^{2-}	540	0.0056	2673
K^+	520	0.0132	429
HCO_3^-	250	0.0040	3143

N = the number of published analyses used to calculate the average

The saline pore fluids in sandstone reservoirs are typically dominated by NaCl with significant $CaCl_2$ and additional K_2SO_4 and $MgCl_2$. Values from the most comprehensive compilation of North American oil-field brine compositions were averaged to obtain the concentrations used for the modeled brine shown in Table 1 (Collins, 1975). These values are the same as used in Balashov et al (2013).

3. Mineralogy, Thermodynamics and Kinetics

In our first model (Balashov et al., 2013), the chemical system simulated was the 8-component system SiO_2-Al_2O_3-CaO-Na_2O-K_2O-HCl-CO_2-H_2O. Here, we extended to the 12-component system, SiO_2-Al_2O_3-CaO-**MgO-FeO**-Na_2O-K_2O-HCl-**H_2SO_4**-CO_2-**O_2**-H_2O (bold components are the new additions). As in our previous paper, a relatively simple baseline sandstone/shale (ss/sh) mineralogy was chosen (Table 2). The sandstone mineralogy was described previously (Balashov et al., 2013). The shale mineralogy (Hosterman and Whitlow, 1983) was chosen to be close to that of a black shale like that of the Marcellus formation (Table 2). We present these baseline mineralogies in the hope that other modellers will benchmark their models against these systems.

Table 2. Mineral compositions of sandstone and shale

Minerals	*Formula*	Sandstone		Marcellus Shale	
		mass %	volume %	mass %	volume %
Primary					
Quartz	SiO_2	65	48.75	38	38.41
Microcline	$KAlSi_3O_8$	18	13.5	2	2.10
Oligoclase	$Ca_{0.2}Na_{0.8}Al_{1.2}Si_{2.8}O_8$	8	6	0	0
Calcite	$CaCO_3$	5	3.75	5	4.93
Smectite	$K_{0.05}Ca_{0.5}Al_{2.8}(Fe_{0.5}Mg_{0.7})Si_{7.65}Al_{0.35}O_{20}(OH)_4$	3	2.25	0	0
Illite[a]	$KAl_3Si_3O_{10}(OH)_2$	1	0.75	35	33.13
Pyrite	FeS_2	0	0	5	2.67
Chlorite	$Mg_{2.7}Fe_{1.8}Fe^{III}_{0.12}Al_{1.38}[Al_{1.5}Si_{2.5}O_{10}(OH)_8]$[b]	0	0	15	13.76
Porosity	volume %	25		5	
Secondary minerals that may form					
Albite	$NaAlSi_3O_8$	0		0	
Kaolinite	$Al_2Si_2O_5(OH)_4$	0		0	
Ankerite	$CaFe_{0.6}Mg_{0.4}(CO_3)_2$	0		0	

Siderite	$FeCO_3$	0	0
Dolomite	$CaMg(CO_3)_2$	0	0
Goethite	FeOOH	0	0
Magnetite	Fe_3O_4	0	0

[a] Including mica
[b] Lowson et al. (2005)

The apparent Gibbs free energies of minerals and aqueous species are represented in Table S1 (Supplementary Information).

The rate I_m of a heterogeneous reaction mineral/fluid is written following transition state theory according to the equation which has been reviewed many times in the literature (BRANTLEY, 2008):

$$I_m = s_m k_m (1 - \exp(-A_m / RT)) \qquad m = 1, 2, ..., N_m \tag{1}$$

In this equation s_m is the specific surface area of mineral m (m^2 m^{-3}). A_m in Equation (1) is the chemical affinity of heterogeneous reaction (S1) which is included so that rate law (1) describes mineral dissolution if $A_m > 0$ and mineral precipitation if $A_m < 0$. The value k_m in Equation(1) is the reaction kinetic constant.

The k_m in rate laws describing mineral dissolution/precipitation (Equation 1) were formulated following a published approach (Brantley, 2008; Köhler et al., 2003; Lowson et al., 2007; Lowson et al., 2005; Marini, 2007; Palandri and Kharaka, 2004). The kinetic function for mineral m is expressed as the sum of three contributions

$$k_m = k_{H,m} + k_{W,m} + k_{OH,m} \tag{2}$$

where

$$k_{H,m} = a_{H^+}^{n_{H,m}} A_{H,m} \exp\left(-\frac{E_{H,m}}{RT}\right) \tag{3}$$

$$k_{W,m} = A_{W,m} \exp\left(-\frac{E_{W,m}}{RT}\right) \tag{4}$$

$$k_{OH,m} = (b_{H,m} a_{H^+}^{n_{OH,m}} + b_{OH,m} a_{OH^-}^{n_{OH,m}}) A_{OH,m} \exp\left(-\frac{E_{OH,m}}{RT}\right) \tag{5}$$

Subscripts H, W, and OH refer to proton-, water-, and hydroxyl-promoted dissolution respectively. This approach uses three activation energies $E_{H,m}$, $E_{W,m}$, and $E_{OH,m}$ to describe these three mechanisms of dissolution, respectively. In some cases in the literature (Palandri and Kharaka, 2004), the hydroxyl-promoted mechanism is written using the term $a_{H^+}^{n_{OH}}$, while in other cases (Brantley, 2008; Köhler et al., 2003) with $a_{OH^-}^{n_{OH}}$. For this reason, in Equation (5) the coefficients b_H and b_{OH} equal either 0 or 1. In other words, either term can be used (but not both) depending upon how the original authors parameterized their model. The parameters used in Equations (2) – (5) are represented in Table 4. As described later, these kinetic constants were varied in sensitivity tests to assess how kinetics affected the CO_2 storage.

Table 3. Dissolution rate parameters for minerals[1]

Mineral	Acidic Mechanism			Neutral Mechanism				Basic Mechanism		
	E_H kJ mol^{-1}	A_H mol m^{-2}s^{-1}	n_H	E_W kJ mol^{-1}	A_W mol m^{-2}s^{-1}	E_{OH} kJ mol^{-1}	A_{OH} mol m^{-2}s^{-1}	n_{OH}	b_H	b_{OH}
Quartz	-	-	-	87.6	22.91	108.37	10	-0.5	1	0
Albite	65	33.11	0.46	69.8	1.55	71	$2.88\ 10^{-5}$	-0.572	1	0
Microcline	51.7	0.1	0.5	38	$1.78\ 10^{-6}$	94.1	$1.95\ 10^{-5}$	-0.823	1	0
Oligoclase	65	52.48	0.46	69.8	2.45	-	-	-	-	-
Calcite	14.4	165.96	1	23.5	0.02	-	-	-	-	-
Smectite	23.6	$1.41\ 10^{-7}$	0.34	35	$2.24\ 10^{-7}$	58.9	$6.31\ 10^{-7}$	-0.4	1	0
Illite[2]	46	$2.2\ 10^{-4}$	0.6	14	$2.5\ 10^{-13}$	67	0.27	0.6	0	1
Kaolinite	65.9	1.74	0.78	22.2	$5.13\ 10^{-10}$	17.9	$1.23\ 10^{-14}$	-0.472	1	0
Chlorite[3]	60	5.27	0.49	60	$3.25\ 10^{-3}$	60	$5.27\ 10^{-7}$	-0.43	1	0
Dolomite	36.1	$1.36\ 10^{3}$	0.5	52.2	$4.12\ 10^{1}$	-	-	-	-	-
Ankerite[4]	36.1	$1.36\ 10^{3}$	0.5	52.2	$4.12\ 10^{1}$	-	-	-	-	-
Siderite[5]	14.4	$1.39\ 10^{-4}$	1	23.5	$5.98\ 10^{-6}$	-	-	-	-	-
Magnetite	18.6	$4.66\ 10^{-6}$	0.28	18.6	$3.01\ 10^{-8}$	-	-	-	-	-
Goethite	-	-	-	86.5	$1.64\ 10^{7}$	-	-	-	-	-
SC CO_2[6]	-	-	-	-	$2\ 10^{-2}$	-	-	-	-	-

[1]All parameters from Palandri and Kharaka (2004) unless noted otherwise.

[2]Köhler et al. (2003).

[3]Lowson et al. (2005, 2007).

[4]Chosen to be identical to dolomite (Palandri and Kharaka, 2004).

[5]Chosen to be identical to magnesite (Palandri and Kharaka, 2004).

[6]Based on Shindo et al. (1995).

The kinetic law represented by Equations (1 – 5) does not take into account explicitly the activities of dissolved aqueous species other than H^+ and OH^-. A more general and inclusive approach might consider the influence of other dissolved species on kinetics, for example Al^{3+} (OELKERS, 2001). However, such effects generally result in an effect within 1 order of magnitude on the apparent rate constant (SCHOTT et al., 2009) and are thus considered to be part of the reason we pursue sensitivity testing on the rate constants.

In many experimental works on mineral dissolution kinetics, a highly nonlinear dependence of dissolution rate on chemical affinity A_m has been observed (BURCH et al., 1993; CAMA et al., 2000; MARTY et al., 2011; XU et al., 2012; ZHANG et al., 2015). Our kinetic law (Equation 1) cannot account for these complex effects. However the sigmoidal dependence of dissolution rate on chemical affinity usually leads to a deviation from Equation 1 within 1 order of magnitude

(BURCH et al., 1993; XU et al., 2012; ZHANG et al., 2015). Thus our sensitivity analysis can investigate these effects to some degree.

In the case of chlorite we have used as our standard base case (i.e. before sensitivity testing) the 25°C dissolution rate data reported for iron-rich chlorite (Lowson et al., 2005). The activation energy was estimated as 60 kJ mol^{-1} (Table 3) based on Lowson et al. (2007) data for 25 – 95 °C. In contrast, the recent data for dissolution of magnesium-rich chlorite (Black and Haese, 2014) from 50 to 120 °C and 120 to 200 bar CO_2 was described with a lower apparent activation energy of 16±0.5 kJ mol^{-1}. With this activation energy, the chlorite kinetic constant decreases by one order of magnitude at 75 °C compared to our 'standard' value (Table 4). However, the reactive diffusion model shows that a decrease in the chlorite kinetic constant by 10x does not change the output in any essential way because chlorite always remains close to local equilibrium (see below).

The most accurate kinetic laws for pyrite dissolution are formulated as functions of pH, activities of aqueous ferric ion, and dissolved oxygen (McKibben and Barnes, 1986; Rimstidt and Newcomb, 1993; Williamson and Rimstidt, 1994). Our calculations showed that under our model conditions these activities were too small (Table 5) to promote a significant rate of pyrite dissolution even though the pore brine in the shale is always undersaturated with respect to pyrite. The pyrite was therefore treated in our simulation as an inert mineral.

The SC CO_2 phase was treated as a separate mineral-like phase and Equation (1) was used to describe its dissolution kinetics. The kinetic constant for dissolution of the SC CO_2 was estimated from the work of (SHINDO et al., 1995). This rate constant is reported per m^2 of SC CO_2 - brine interface.

4. Reactive Transport Modeling

To solve the full reaction – diffusion problem, the program, MK76, was utilized for a heterogeneous system of one aqueous and N_m mineral phases including SC CO_2. MK76 forms and solves the system of differential equations in partial derivatives for reactive diffusion mass transfer (Balashov et al., 2013). In all computations the numerical grid consisted of 601 equidistant spatial nodes. To initiate the simulation, the model was parameterized for the sandstone/shale interface. Upon initiation, the sandstone contained supercritical (SC) CO_2 (5 % of rock volume) and brine (20% of rock volume) while the shale contained only brine (5% of rock volume).

In the simulation it was assumed that the gas was injected into a subhorizontal layer of permeable sandstone overlain by low-permeability shale, following the concept described in the literature for most such sequestration (Benson and Cook, 2005). After injection, the supercritical CO_2 plume will form a plume entirely within the sandstone. The fate of this plume depends on the slope of the sandstone layer. If the slope is around 10%, the SC CO_2 theoretically will scatter and become immobilized by capillary forces within 25 a (Doughty, 2010), filling clusters of pores that are disconnected due to brine infilling. In this stabilized state, the CO_2 saturation of the porous medium is called the residual CO_2 saturation (HESSE et al., 2008). After this physical stabilization, the plume will likely consist of a heterogeneous region of pores containing the two immiscible phases: SC CO_2 and CO_2–saturated brine. Our estimate that the residual SC CO_2 phase will constitute 5% of the sandstone volume (where the sandstone porosity equals 25%) is

consistent with a residual CO_2 saturation of 20%. This is a reasonable value taking into account that the high end of most such estimates is typically ~30% (Szulczewski et al., 2012).

On the other hand, if the slope of the reservoir with respect to horizontal is smaller than 10% (Szulczewski et al., 2014) or if the geological structure forms an anticlinal dome with overlying impermeable sediments (Pearce et al., 1996), then a continuous CO_2 plume can exist through many millennia. For example, new calculations for the Bravo Dome natural CO_2 gas reservoir are consistent with a large CO_2 plume existing for up to 1.2 Ma (Sathaye et al., 2014). If similar geological place will be chosen for CO_2 sequestration the presence of wellbores can facilitate the CO_2 leakage (JORDAN et al., 2015).

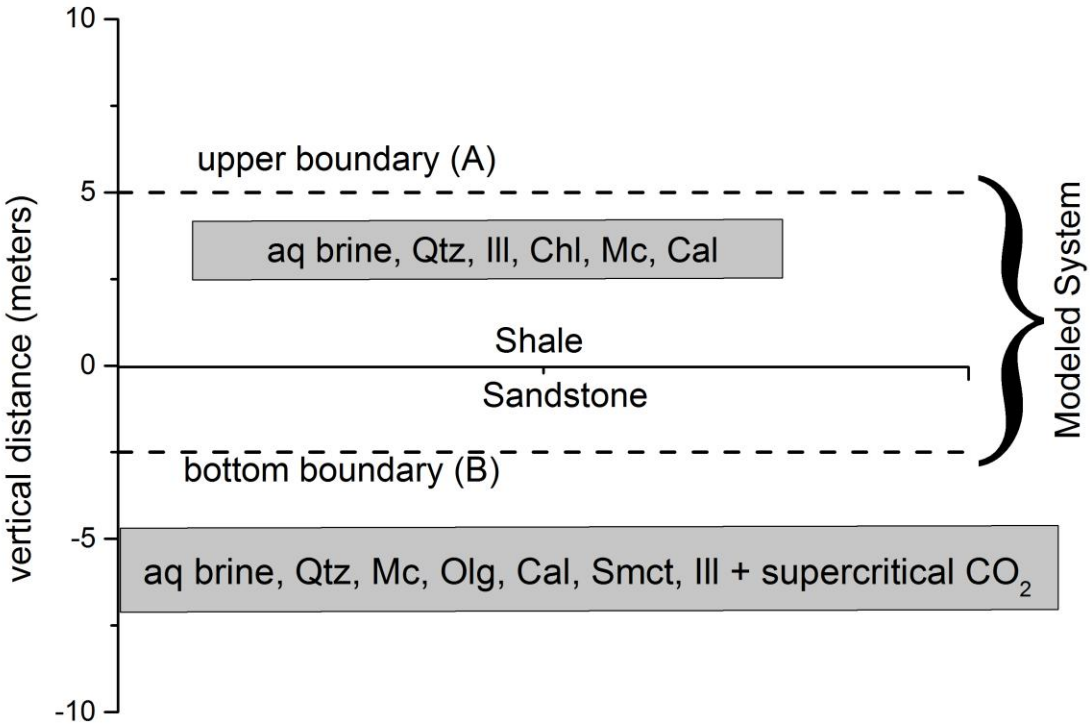

Figure 1. Setup of the reactive diffusion model for the contact between the reservoir (sandstone)/ caprock (shale). The boundaries are labeled: upper boundary (A) and bottom boundary (B). Five percent of the initial sandstone porosity (which has a total porosity of 25%) is filled by supercritical CO_2.

Within the upper part of the plume, the CO_2 diffuses into the shale caprock (Gaus et al., 2005) (Figure 1). The content of water in the SC CO_2, assumed to be negligible, was set to zero. This is reasonable in that at 75 °C and 30 MPa, SC CO_2 fluid is calculated to contain only ~0.6 mass % H_2O after equilibration with the brine (Duan and Sun, 2003).

Rock porosity, effective rock diffusivity and permeability are important in determining CO_2 storage. These parameters are reservoir-specific and can vary significantly within a reservoir. Fick's first law for diffusion through porous media for 1 dimension is

$$j = -F_{inv} D_{aq} \frac{\partial c}{\partial x} \qquad (6)$$

where j is diffusion flux per 1 m^2 of rock [mole $m^{-2}s^{-1}$], and D_{aq} is the diffusion coefficient in pore solution [m^2s^{-1}]. The geometrical effects of pore connectivity, effective pore cross section, and pore tortuosity are generally modeled using the inverse of the Archie formation factor F_{inv} (Balashov et al., 1983). The dependence of F_{inv} on porosity (ϕ) can be represented as the Archie power law (Archie, 1942; Boving and Grathwohl, 2001; Brace, 1977; Jacquier et al., 2013) which can be written in an extended form as:

$$F_{inv} = \alpha \phi^{n_F} \qquad (7)$$

Here this factor is approximated using $\alpha = 1/\theta_\tau$, where the tortuosity coefficient $\theta_\tau = \pi/2$ for packed spheres, and n_F is equal to 1 for sandstone and 1.5 for shale. The "standard" n_F = 1.5 is based on data for igneous rocks of low permeability (Balashov and Zaraisky, 1982; Zaraisky and Balashov, 1995). For porosities of sandstone of 0.25 and shale of 0.05, the inverse factor equals 0.16 and 0.007, respectively (i.e. the ss/sh ratio of inverse factors = 22.7). This F_{inv} value for shale is consistent with reported effective diffusion measurements of heavy (D_2O) and tritiated (HTO) water in shale: e.g., F_{inv} values around 0.004 have been reported for caprocks of 6% porosity (Berne et al., 2010; Fleury et al., 2009). Other researchers used diffusion data for HTO and $^{36}Cl^-$ in clay rocks and Equation (15) to estimate $\alpha = 0.17$ and $n_F = 1.6$, consistent with our estimates (Jacquier et al., 2013). Values of n_F about 2 – 2.5 for compact sedimentary rock were reported by (ULLMAN and ALLER, 1982; VAN LOON et al., 2003).

5. Model Geometry

The model geometry was represented by two horizontal rock layers: 2.5 m of sandstone and 5 m of shale (Figure 1). The upper boundary (A) was modeled as a no-flux boundary for all species. The bottom boundary (B) was no-flux boundary for all components except $CO_{2,aq}$ and $O_{2,aq}$, i.e., the concentrations of $CO_{2,aq}$ and $O_{2,aq}$ at B were maintained constant. The thicknesses of these layers were considered to be large enough to characterize the reactive process focused at the ss/sh contact. The concentration of $CO_{2,aq}$ at B was set close to the value calculated after equilibration with the initial brine for the SC CO_2 phase at 75 °C and 30 MPa ($m^A_{CO2,aq}$= 0.7434 mole kg^{-1}). The $O_{2,aq}$ molality was maintained constant at 7.4×10^{-9} mole kg^{-1}. This value is equivalent to 0.24 ppb dissolved O_2 and it corresponds to the lower limit of detection using standard analytical determination. We have chosen this value in acknowledgement that some small amount of O_2 can be mixed with CO_2 during injection.

6. Results: The Standard Case

The initial composition of the sandstone and shale pore fluids (Table S2) were calculated by equilibrating the composition of the average brine (Table 1) with the sandstone and shale minerals respectively (Table 2). The presence of capillary-trapped SC CO_2 (5 volume %) in the sandstone was ignored at the initial chemical equilibrium calculations. Throughout the rest of the simulation, the mineralogy across the sandstone remains relatively uniform, so the evolution in sandstone mineralogy was represented by changes in mineral abundances averaged across the sandstone (Figure 2a, bottom panel). In contrast, the reaction in the shale is focused in a narrow zone at the ss/sh interface. Most of the alteration occurs within 1 m of the contact and especially within a thin shale sub-layer at the interface. In our calculations, the minimal accessible thickness of the interface of the shale sub-layer was defined by the spatial grid -- and was equal to 1.25×10^{-2} m. The average mineral concentrations in these shale sub-layers are plotted in Figure 2a (top and middle panels).

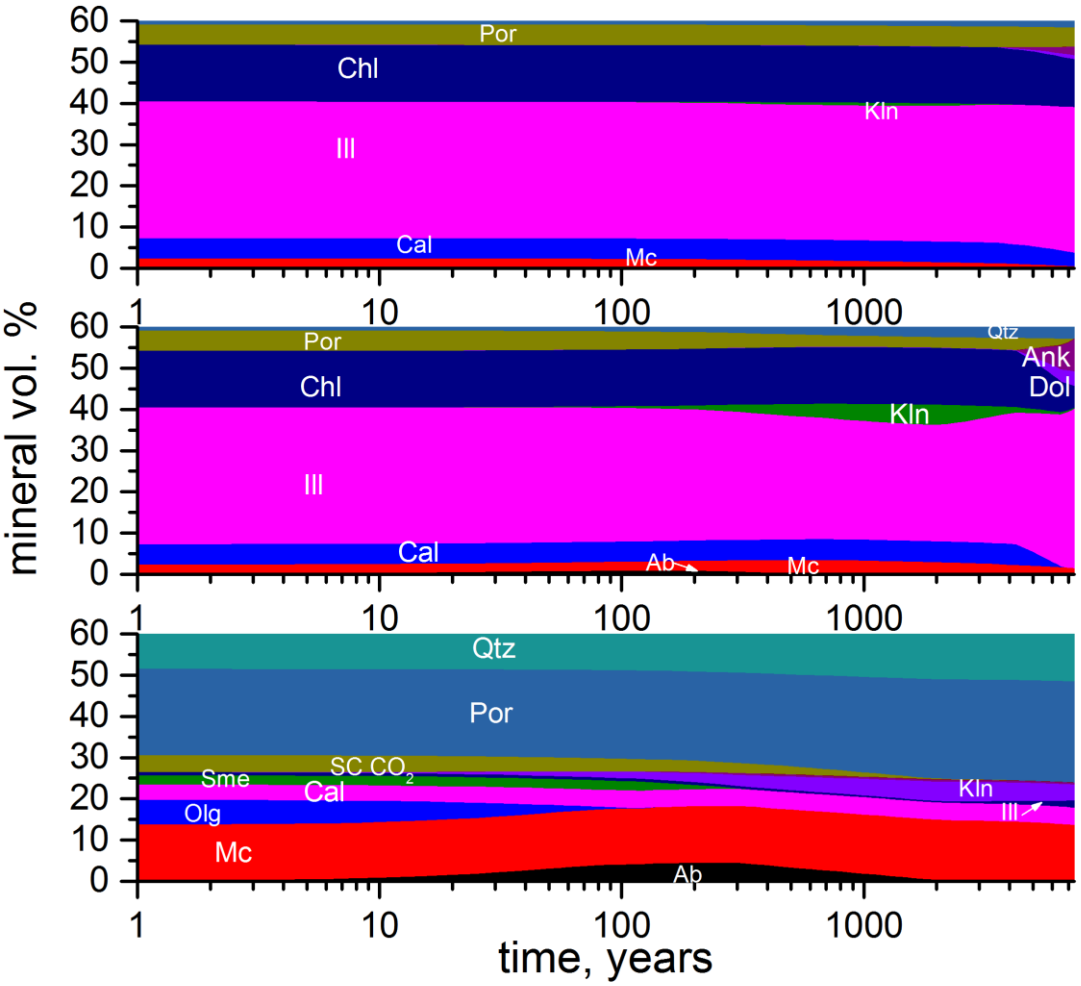

2a)

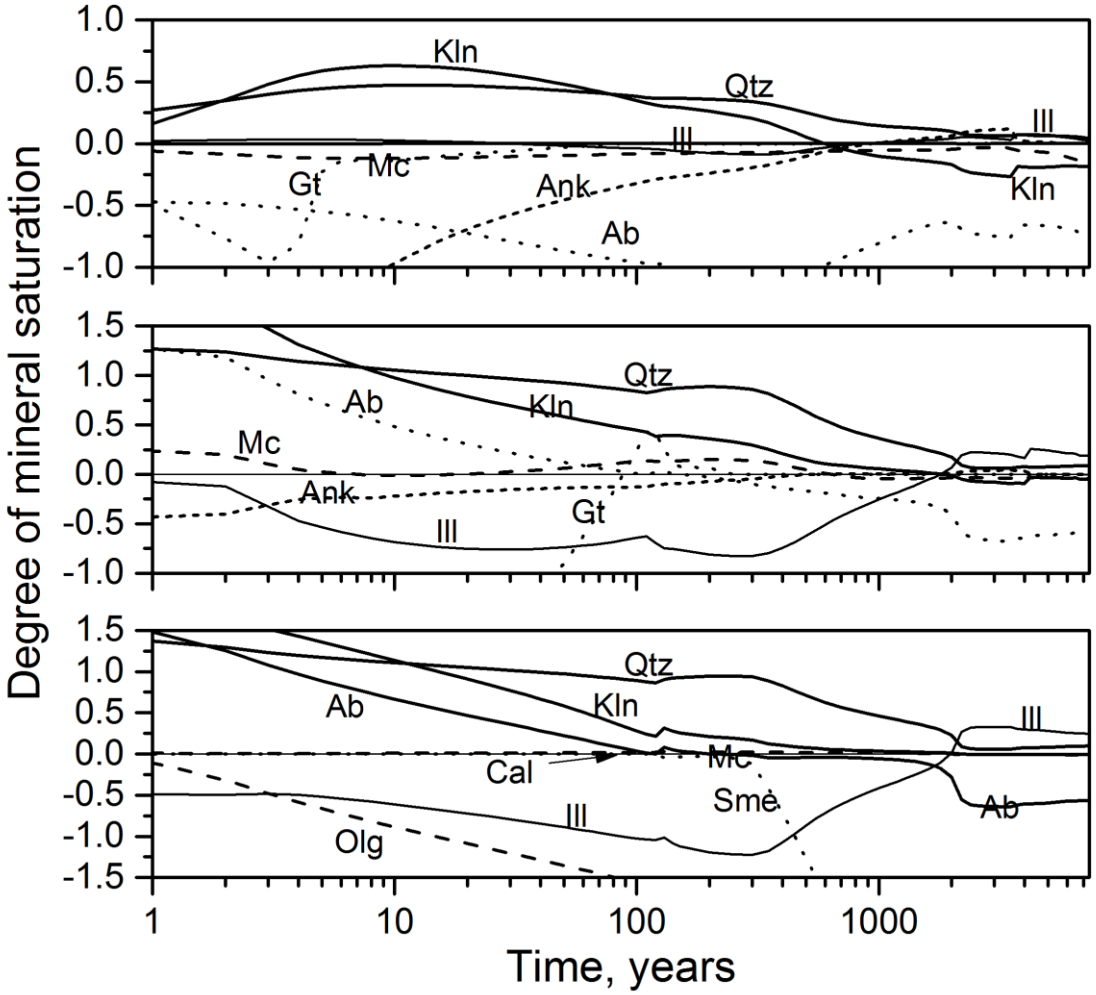

2b)

Figure 2. The time evolution of (a) the average mineral volume fraction and (b) the average saturation indices (log (Q/K_{eq})) for the standard model simulations in three parts of the system: in a 1-meter sub-layer defined from the interface inward into the shale (top), in the shale exactly at the sandstone / shale interface (middle), and in a 2.5 m layer of sandstone (bottom). Acronyms are defined as follows: Por = porosity, Chl = chlorite, Qtz = quartz, Ank = ankerite, Dol= dolomite, Kln = kaolinite, Ill= illite, Cal = calcite, Ab = albite, Mc= microcline, SC CO_2 = supercritical CO_2, Sme = smectite, Olg = oligoclase, Gt = goethite. Here, Q is the ion activity product for each reaction and K_{eq} is the chemical equilibrium constant for each reaction: saturation indices = 0 at equilibrium.

The time evolution of the saturation indices for minerals in the three sub-layers are shown in Figure 2b. The fast dissolution of SC CO_2 in sandstone brine changes its pH from the initial 7.8

(Table S2) to 5 after 1 year and promotes the remarkable deviation from equilibrium for initially equilibrated minerals such as quartz and illite (Figure 2b, bottom). The middle (the thin ss/sh interface) and bottom panels (ss layer) have many similarities. In both cases an inversion occurs in the kaolinite and illite saturation curves at ~ 2000 a – i.e. kaolinite precipitation switches to dissolution and illite dissolution switches to precipitation. Before this point, the brine is supersaturated in kaolinite and undersaturated in illite but the reverse is true after this point. This coupled behavior of Kln / Ill is accompanied by a decrease in quartz supersaturation (Figure 2b, middle and bottom) and an increase in potassium activity with time.

With respect to porosity, perhaps the most important mineral is ankerite. In contrast to calcite and dolomite which are always at local equilibrium, ankerite is strongly undersaturated during the first 600 a (Figure 2b, top and middle), then approaches local equilibrium until 2000 a, and then is supersaturated from 2000 to 3500 a (Figures 2a and 2b, top and middle). Precipitation of ankerite eventually completely seals the porosity at the ss/sh interface (7416 a).

CO_2 is trapped in the sandstone by both mineral and solubility trapping and is controlled most directly by the reactions of oligoclase, smectite and albite. Specifically, trapping of CO_2 is determined by dissolution of oligoclase and release of Ca, the replacement of smectite by calcite and dolomite, and by the dissolution of albite which releases Na and drives precipitation of kaolinite. The first two reactions control concentrations of Ca in solution (which controls mineral trapping by affecting the solubility index of calcite) and the latter reaction controls the conversion of $CO_{2,aq}$ into HCO_3^- (solubility trapping). The bicarbonate in solution largely balances the Na^+ released from feldspar. Mineral trapping of CO_2 essentially stops by 1000 a. By ~ 2000 a, albite disappears (Figure 2a, bottom) and CO_2 solubility trapping reaches its maximum. After that time, formation of bicarbonate continues at a very slow rate due to the very slow kinetics of kaolinite + microcline replacement by illite. Eventually, final equilibration produces the assemblage, Mc+Ill+Cc+Dol+Qtz.

Different reactions take place in the shale layer. The average concentrations of CO_2 (mol per m^3) accumulated in the 0 – 5 m shale layer are plotted versus time in Figure 3 (top). Up to 3500 a, the mineral that traps CO_2 in the shale is mostly dolomite. From 3500 to 7416 a, intensive ankerite and dolomite precipitation is accompanied by calcite dissolution (Figure 3, top).

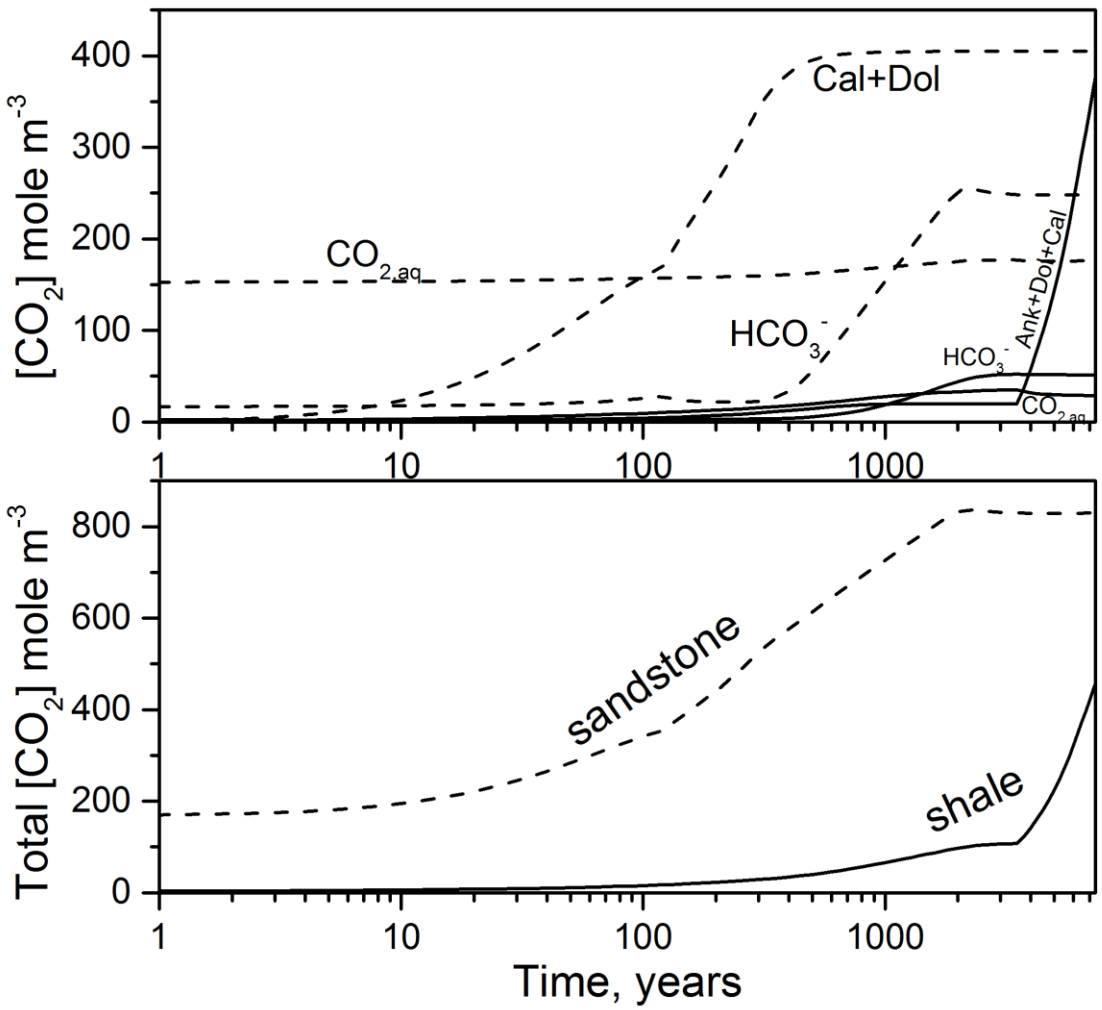

Figure 3. The average CO_2 accumulated per m^3 of the sandstone in 2.5 m layer of sandstone (dashed line) and in 5 m layer of shale 5 m (solid line) plotted versus time. Top graph: lines depict solubility-trapped molecular CO_2 in brine ($CO_{2,aq}$), solubility-trapped CO_2 as HCO_3^-, and mineral-trapped CO_2 due to carbonate precipitation (ankerite (Ank), dolomite (Dol), calcite (Cal)). Bottom graph: the total accumulation of CO_2 in sandstone and shale summed over all mechanisms shown in the top graph. The termination time (7416 a) corresponds to the point of complete shale porosity sealing at the ss/sh interface.

Solubility trapping of CO_2 in the 5 meter-thick shale is small in comparison to the sandstone because of the small porosity (Figure 3, top). The total CO_2 trapped in shale up until the point of porosity occlusion at the ss/sh interface is ~2 times less than the amount stored in the sandstone (Figure 3, bottom). However, if we were to assume a sandstone layer of 100 m thickness, the amount of CO_2 trapped in shale caprock would be an even more minimal contribution (1.3% of CO_2 stored in the sandstone reservoir).

7. Reactive Zone in Shale

It is clear from Figure 2 that the reactions in shale seal the porosity very close to the ss/sh contact. This happens because of the contrast in the sandstone and shale mineralogies: the relatively high abundances of oligoclase and smectite in the sandstone and chlorite content (> 5 %) in the shale. Specifically, oligoclase and smectite provide the Ca and Mg, and chlorite provides the Fe and Mg that drive precipitation of the calcite, dolomite and ankerite. Others have investigated porosity closure at the interface of rocks of differing mineralogy undergoing metasomatism (BALASHOV and LEBEDEVA, 1991; ZARAISKY et al., 1989; ZARAISKY et al., 1986). Such porosity clogging is important, for example, where hyper-alkaline solutions or cement-based materials are in contact with clay-containing rocks (LICHTNER et al., 1998; STEEFEL and LICHTNER, 1994; STEEFEL and LICHTNER, 1998). This topic is also now being investigated more thoroughly (Cochepin et al., 2008; Lagneau and Lee, 2010; Marty et al., 2010; Marty et al., 2009; Shao et al., 2013).

The important mineral-fluid reactions in the modeled sandstone and shale are summarized below. In the sandstone three acid-base reactions are important:

1. oligoclase dissolution

$$\mathrm{Olg} + 1.2\mathrm{CO_{2,aq}} + 2.4\mathrm{H_2O} \rightarrow 0.2\mathrm{Ca^{2+}} + 0.8\mathrm{Na^{+}} + 1.2\mathrm{Al(OH)_{3,aq}} + 2.8\mathrm{SiO_{2,aq}} + 1.2\mathrm{HCO_3^-} \quad (8)$$

2. albite precipitation

$$\mathrm{Na^{+}} + \mathrm{Al(OH)_{3,aq}} + 3\mathrm{SiO_{2,aq}} + \mathrm{HCO_3^-} \rightarrow \mathrm{Ab} + \mathrm{H_2O} + \mathrm{CO_{2,aq}} \quad (9)$$

3. albite incongruent dissolution with kaolinite formation

$$\mathrm{Ab} + \mathrm{CO_{2,aq}} + 1.5\mathrm{H_2O} \rightarrow \mathrm{Na^{+}} + 0.5\mathrm{Kln} + 2\mathrm{SiO_{2,aq}} + \mathrm{HCO_3^-} \quad (10)$$

Two acid-base reactions are important in both sandstone and shale:

1. microcline dissolution

$$\mathrm{Mc} + \mathrm{CO_{2,aq}} + \mathrm{H_2O} \rightarrow \mathrm{K^{+}} + \mathrm{Al(OH)_{3,aq}} + 3\mathrm{SiO_{2,aq}} + \mathrm{HCO_3^-} \quad (11)$$

2. kaolinite replacement by illite and vice versa

$$3\mathrm{Kln} + 2\mathrm{K^{+}} \rightleftarrows 2\mathrm{Ill} + 3\mathrm{H_2O} + 2\mathrm{H^{+}} \quad (12)$$

Finally, the important reaction in the shale is carbonation of chlorite coupled with calcite dissolution and dolomite precipitation:

$$\mathrm{Chl} + 4.5\mathrm{Cal} + 0.38\mathrm{SiO_{2,aq}} + 0.96\mathrm{K^{+}} + 0.96\mathrm{HCO_3^-} + 3.54\mathrm{CO_{2,aq}} \rightarrow 0.96\mathrm{Ill} + 3\mathrm{Ank} + 1.5\mathrm{Dol} + 0.12\mathrm{Gt} + 3.46\mathrm{H_2O} \quad (13)$$

The importance of the last reaction for CO_2 consumption by shale and the reduction of porosity in shale was underlined by previous workers (Rochelle et al., 2004). The onset of this reaction at 3600 a marks the beginning of formation of a reactive zone in the shale at the ss/sh

interface. At 3500 a, reaction (10) has not yet started and the sandstone brine has greater concentrations of $Al(OH)_{3,aq}$, Mg^{++} and Ca^{++} than the shale brine, but the Fe^{++} molality is greater in the shale brine. For this reason, the shale brine at the ss/sh interface is supersaturated with respect to ankerite at this time (Figure 2b, top and middle).

The solid volume change due to progress of reaction (13) equals 51.365 cm^3 per mole of Chl. However this positive change can explain only 1.53 % of the porosity decrease for our simulation (i.e., where the initial shale porosity = 5%), under the assumption that no Ca or Mg are transported into the reactive zone (initial calcite concentration = 4.93 vol. %). Additional transport of Ca into the reactive zone of the shale is needed to explain the full porosity closure of the shale at the ss/sh interface (Figure 4a). Namely 23.3 mole % of the Ca in carbonates that occludes the porosity of the shale must be brought in. The inference from this is that the occlusion of porosity is not driven by one single reaction. Instead there is a set of parallel reactions which occlude porosity (Supplementary Information).

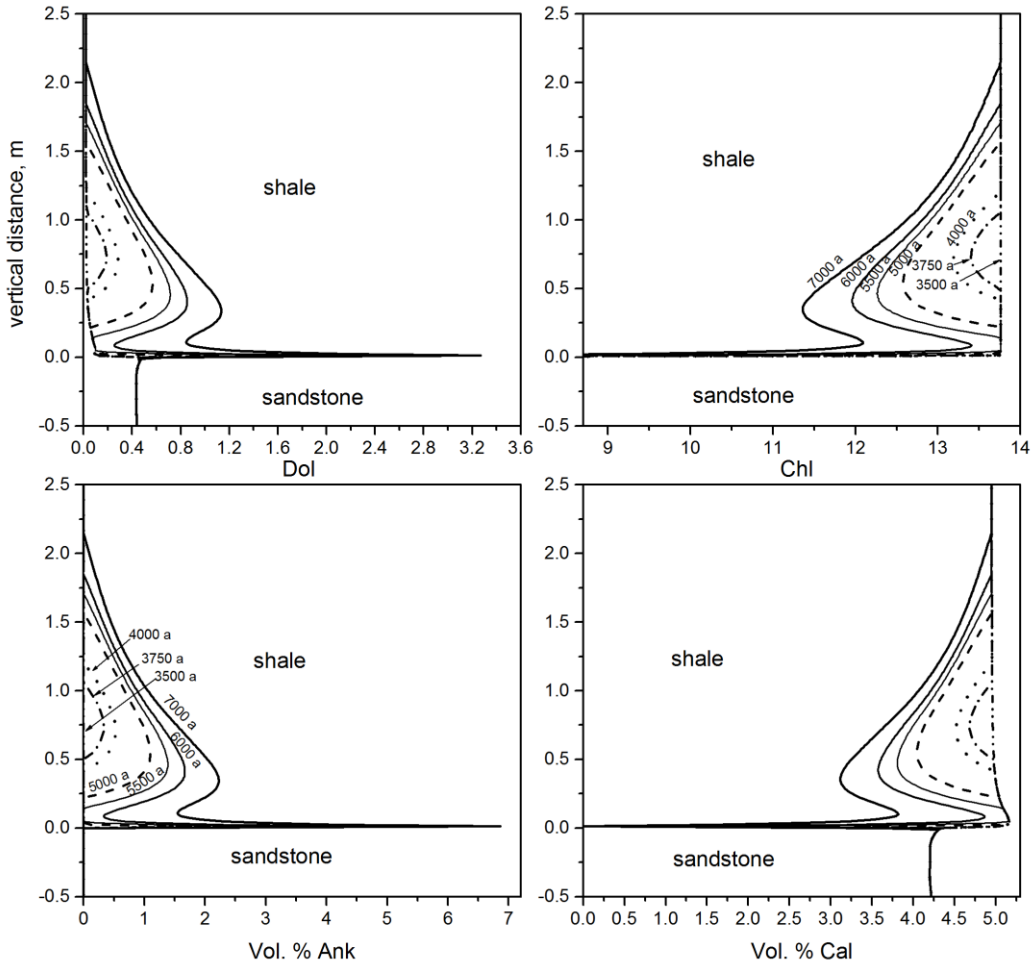

4a)

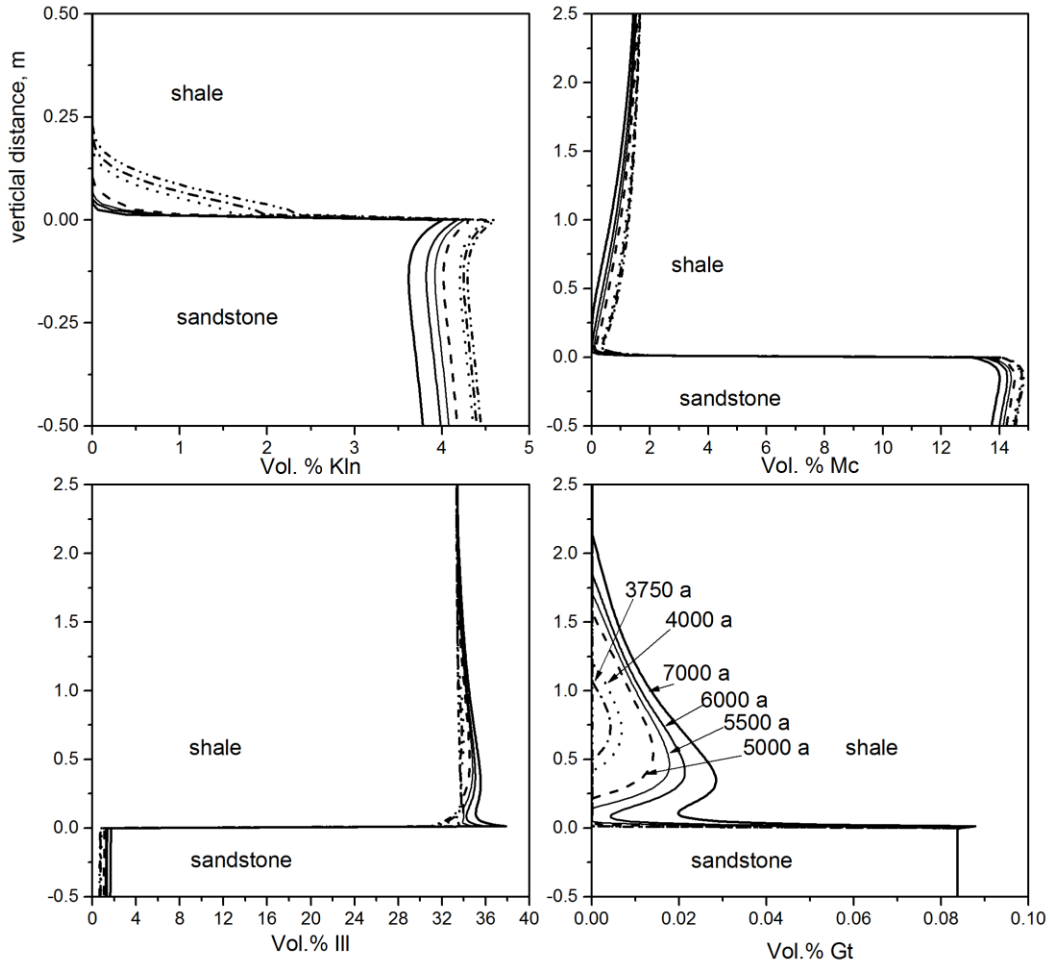

4b)

Figure 4. a) Mineral precipitation (ankerite, dolomite) and dissolution (chlorite, calcite) in the shale reactive zone for times between 3500 and 7000 a after beginning of calculations. b) Mineral precipitation (illite, goethite) and dissolution (kaolinite, microcline) in the shale reactive zone for times between 3500 and 7000 a. With this simulation under standard kinetics, complete porosity closure occurs at the ss/sh interface at 7416 a.

The spatial distributions of minerals in the reactive zone are plotted as a function of time in Figure 4. After 4000 a, ankerite precipitates in the shale at the ss/sh interface (Figure 4a). This precipitation occurs with dolomite precipitation as well as chlorite and calcite dissolution (Figure 4a), microcline dissolution and illite and goethite precipitation (Figure 4b). The whole process proceeds in time after the Kln/Ill inversion at 2000 a (Figure 2, Figure 4b). Throughout, calcite, ankerite, dolomite, chlorite and goethite are all at local chemical equilibrium with brine, and

microcline is close to local equilibrium (Figure 2b, 4). Thus the most important control on reaction progress is the kinetics of illite precipitation. The overall mineral reaction for the shale reactive zone can be expressed as the sum of reactions (12) and (13):

$$\begin{aligned} &\mathrm{Chl} + 4.5\mathrm{Cal} + 0.96\mathrm{Mc} + 4.5\mathrm{CO}_{2,\mathrm{aq}} \rightarrow \\ &0.96\mathrm{Ill} + 3\mathrm{Ank} + 1.5\mathrm{Dol} + 0.12\mathrm{Gt} + 0.96\mathrm{Al(OH)}_{3,\mathrm{aq}} + 2.5\mathrm{SiO}_{2,aq} + 2.5\mathrm{H}_2\mathrm{O} \end{aligned} \quad (14)$$

The delay in onset of reaction (13) is related to the delay in ankerite precipitation from the supersaturated fluid. This latter delay is related to the time dependence of the ankerite saturation index (Figure 2b). In the algorithm implemented in MK76 to model minerals such as ankerite that precipitate but are not present initially, the mineral must be included in the initial system at a nominal concentration (1 ppm in volume fraction units). The mineral specific surface area is calculated from the mineral volume fraction raised to a power, where the power changes from 2/3 to 5/3 for mineral volume fractions less than 1 ppm. By using this algorithm for mineral appearance/disappearance, there was no delay in mineral precipitation for albite, kaolinite, dolomite and goethite. The ankerite delay occurs because of its long period of strong undersaturation (600 a, Figure 2b). During this period of undersaturation, the ankerite volume fraction drops below 1 ppm. Ankerite precipitation in the shale first begins at some distance from the ss/sh contact at a location where the threshold is reached first (for time 3750 a at 0.5 – 1 m in Figure 4a). Only after some span of time does intensive ankerite precipitation begin at the ss/sh interface. For time 4000 a in Figure 4a, the distribution of ankerite precipitation is bimodal – occurring at the ss/sh interface and in the interval 0.6 – 1.1 m. The large second derivative of calcium concentration in the pore fluid at the ss/sh contact leads to a maximum in the rate of ankerite precipitation at that point (Suppl. Inf., Figure S1; Figure 4a).

Although the model parameters of this approach to simulate nucleation and growth of a mineral are somewhat artificial, it makes physical sense that the ease of mineral precipitation depends on the initial concentration of a mineral (Lüttge et al., 2013; Steefel and VanCappellen, 1990). In addition, ankerite formation in sedimentary rocks in some cases is delayed (Na et al., 2011), and it may therefore be difficult to nucleate (Adabi and Rao, 2003; Milliken, 2002). In some cases, dolomite may act as a mineral precursor to ankerite (Ferry et al., 2009). Likewise, modeling here shows that dolomite precipitates and always accompanies ankerite precipitation (Figure 4a).

The bimodal distribution predicted here for ankerite precipitation resembles Liesegang banding (Lebedeva et al., 2004). For example at 5000 and 5500 a (Figure 4a), two ankerite bands are predicted near and far from the ss/sh interface. All other reactive minerals follow the spatial bimodal ankerite distribution (Figure 4) because they participate in net carbonation reactions of type (13 - 14).

8. Variation of the Transport Properties of the Shale Porous Medium

To explore the influence of F_{inv} on the reactive process at the ss/sh contact, the parameters α and n_F in Equation (7) were varied. In the standard case the values were set to $\alpha = 2/\pi$, $n_F = 1.5$.

The calculations were also completed for $\alpha = 0.09\times 2/\pi$ and $0.03\times 2/\pi$ at $n_F = 1.5$. Simulations were also completed for $n_F = 2$ and $n_F = 2.5$ at $\alpha = 2/\pi$. All the new values for α and n_F decrease the value of F_{inv} and, consequently, the value of the effective diffusion coefficient in the shale, i.e., $D_{eff} = F_{inv} D_{aq}$. In these sensitivity tests, the zone of reaction in the shale contracts compared to the standard case, i.e., this length scale of reaction varies as $\sqrt{D_{eff} t}$.

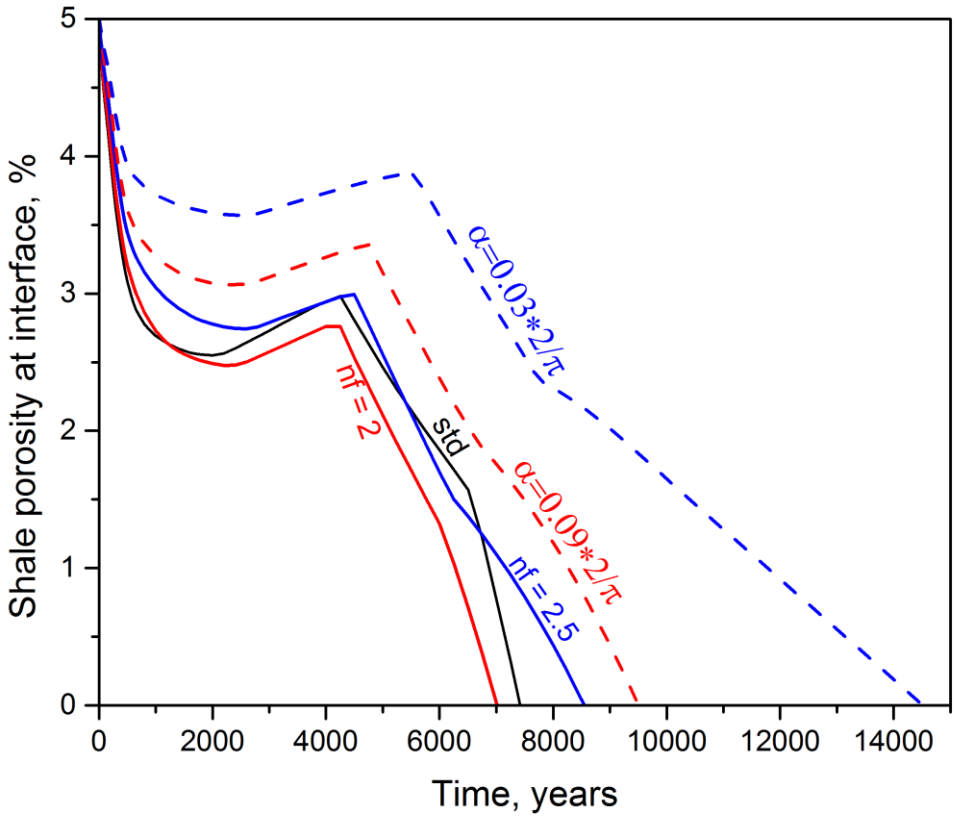

Figure 5. Curves depicting the time evolution of porosity closure as a function of various formation factors for Archie's law as shown in labels (see text for further explanation).

The termination time (time to porosity sealing) is increased when α decreases (Figure 5): 9500 and 14500 a for $\alpha = 0.09\times 2/\pi$ and $0.03\times 2/\pi$, respectively. Changes in the value n_F in Equation (7) influences reactive diffusion in a more complex manner – this is because porosity is itself a function of time and space. An increase in n_F will not only decrease F_{inv} according to Archie's law (7) but will also positively affect mineral precipitation rates at the ss/sh interface. When n_F is increased at constant α, the reaction and porosity occlusion become more focused at the ss/sh interface (Figure 5). As shown in Figure 5, termination times are 7000 and 8500 a at $n_F = 2$ and $n_F = 2.5$, respectively. In all cases where α and n_F were varied, the total CO_2

accumulated in the shale was less than 50% of the calculated CO_2 accumulated in the standard case.

9. Results of Variation in Mineral Kinetics

Five of the minerals do not remain near local chemical equilibrium at the ss/sh interface (Figure 2b): quartz, albite, microcline, kaolinite and illite; goethite approaches local equilibrium after 200 a. Given that quartz content (65 mass % in sandstone and 38% in shale, Table 2) remains essentially unchanged over time, its specific surface area stays constant. Additionally its kinetic constant is small and well constrained (Palandri and Kharaka, 2004), thus we did not run sensitivity tests on the value of the quartz kinetic constant. However, sensitivity analyses were carried out for feldspars and clay minerals (Figure 6). Variations in the feldspar kinetic constants have only a minor influence on the evolution of porosity closure. In contrast, variation in the kaolinite constant demonstrates a large effect: when the Kln kinetic constant is increased by a factor of 10 (Kln×10), porosity closure occurs after 107 instead of 7416 a.

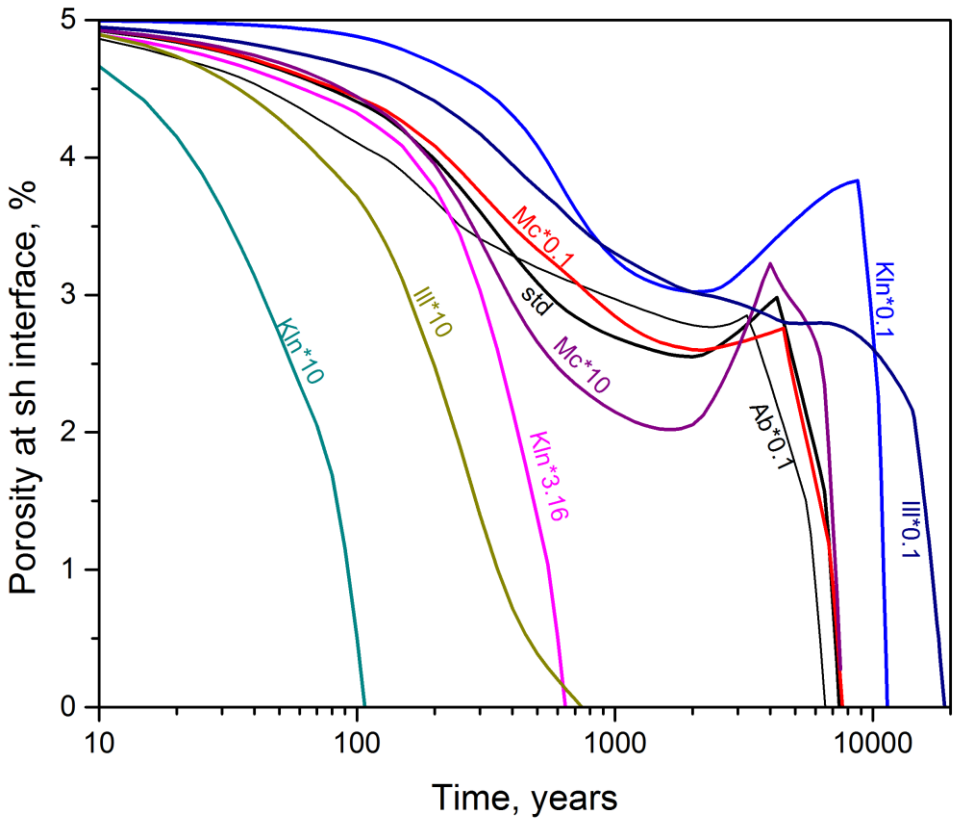

Figure 6. Curves showing the time to porosity closure for different values of the mineral kinetic constants as indicated (where all other contstants were set equal to the standard value). For example, Mc*0.1 is the curve for the time evolution of porosity closure for a simulation

incorporating a microcline kinetic constant equal to 0.1 times that of the standard simulation (i.e. labelled std).

For most cases the initial decrease in shale porosity at the interface (Figure 6) occurs because kaolinite precipitates and illite dissolves. This reaction (Reaction (12)) continues for ~ 2000 a, when the inversion occurs: illite precipitates and kaolinite dissolves, creating porosity. Eventually, ankerite precipitation becomes fast enough that reaction (13) begins, leading to porosity closure (Figures 2, 6). The changes in the mechanism of porosity closure as a function of the variations in kinetic constants of the clay minerals will be discussed later.

To compare the results from the sensitivity tests in the next section, it is convenient to use dimensionless (reduced) time which we define here as

$$\bar{t} = \frac{t}{t_{std}} \tag{15}$$

where t_{std} = 7416 a is the standard termination time when the porosity at the ss/sh interface disappears. Dimensionless quantities of stored CO_2 are also defined for each storage species (subscripts below refer to aqueous CO_2, bicarbonate, mineral trapping, and the total CO_2 trapped (i.e. the sum of all the preceding species)):

$$\begin{aligned}
\bar{S}_{CO_2,aq} &= \frac{[CO_{2,aq}]}{[CO_{2,aq}]_{std}} \\
\bar{S}_{HCO_3^-} &= \frac{[HCO_3^-]}{[HCO_3^-]_{std}} \\
\bar{S}_{CO_2,\min} &= \frac{[CO_{2,\min}]}{[CO_{2,\min}]_{std}} \\
\bar{S}_{CO_2,tot} &= \frac{[CO_{2,tot}]}{[CO_{2,tot}]_{std}}
\end{aligned} \tag{16}$$

In each equation, the entity with subscript "std" refers to the value calculated for the standard case: $[CO_{2,aq}]_{std}$ = 28.79 mol m^{-3}, $[HCO_3^-]_{std}$ = 51.16 mol m^{-3}, $[CO_{2,\min}]_{std}$ = 376.9 mol m^{-3}, and $[CO_{2,tot}]_{std} = [CO_{2,aq}]_{std} + [HCO_3^-]_{std} + [CO_{2,\min}]_{std}$ = 456.85 mol m^{-3}. These values refer to concentrations of the different species of CO_2 per m^3 of shale, i.e., HCO_3^- and $CO_3^=$ dissolved in shale brine, CO_2 trapped in carbonates, and total CO_2 stored in shale for the standard simulation at the termination time.

9.1 *The effects of variations in the feldspar kinetic constants*

Variations in the Ab kinetic constant only affects CO_2 storage in the shale to a minor extent because Ab reactions mostly take place in the sandstone (Balashov et al., 2013). The main influence of the Ab reaction kinetics is that albite reactions affect the pH of the sandstone pore solution. This effect does not significantly affect CO_2 accumulation in the shale.

In contrast to Ab, the kinetic constant for Mc has a greater effect on CO_2 storage in the shale because microcline participates in reaction (14). When the microcline kinetic constant is

decreased 10 times less than its standard value (Mc×0.1), reaction (14) slows. This leads to a 2% increase in the porosity closure time and a 40% decrease in CO_2 accumulation in the shale. In effect, the remained microcline reduces the carbonate content that precipitates at the shale interface.

9.2 *The effects of variations in the clay mineral kinetic constants*

9.2.1 Kaolinite kinetic constant

Given the importance of the kaolinite kinetic constant on CO_2 propagation into the shale, we completed calculations for seven different values of the Kln kinetic constant. The ratios of the Kln kinetic constant (k_{Kln}) to the standard value (k_{Kln}^{std}) were 0.1, 0.316, 0.562, 1, 1.78, 3.16, 10 (i.e., $\log \frac{k_{\mathrm{Kln}}}{k_{\mathrm{Kln}}^{std}}$ = -1, -0.5, -0.25, 0, 0.25, 0.5, 1) as shown in Figure 7. The vertical lines in Figure 7 show the times when porosity closes. CO_2 accumulation at a given time is always the same within 15% for all values of this constant (Figure 7). However, variations in the Kln constant cause changes in the times of porosity closure (Figure 6-7) from 107.5 a at (Kln×10) to 11370 a at (Kln×0.1) so that the maximum amount of CO_2 accumulation in the shale increases. At Kln×0.1, for example, this maximum amount is 60% above the value for the standard case (Figure 7).

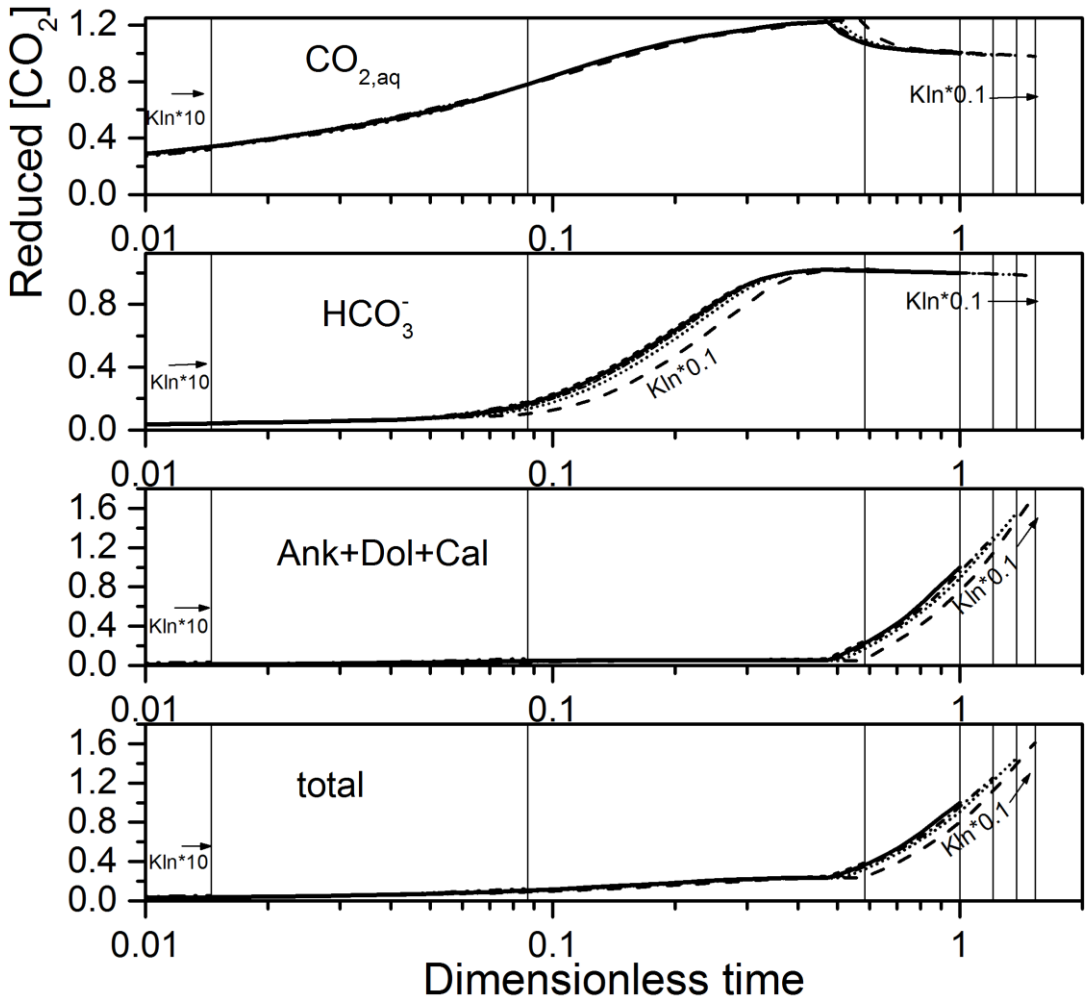

Figure 7. The time dependence of CO_2 accumulation in the shale due to different mechanisms of CO_2 storage. From top to bottom: molecular CO_2 dissolved in brine; CO_2 dissolved in brine as HCO_3^- and $CO_3^=$; CO_2 trapped in mineral carbonates, and the sum total of CO_2 trapped in shale. The vertical lines show the relative termination times for different values of the kaolinite kinetic constant, from left to right: 10 (here the termination time for this simulation = 107.5 a), 3.16, 1.78, 1, 0.562, 0.316, and 0.1. Dotted and dashed lines are simulations with different values of the Kln constant: dot-dashed – 0.562, dotted – 0.316, and dashed – 0.1.

The effect of variation in the Kln constant on mineral saturation within 0.0125 m of the ss/sh interface is shown in Figure 8. Vertical lines in Figure 8 document the termination times for Kln×10, the standard value, and Kln×0.1. For the standard constant, reaction (13) begins at ~ 4000 a with ankerite precipitation, whereas at (Kln×0.1) the same reaction begins at ~ 8500 a. In contrast, at Kln×10 chlorite carbonation begins at ~ 5 a:

$$Chl + 4.5Cal + 0.38SiO_{2,aq} + 4.5CO_{2,aq} \rightarrow 1.44Kln + 3Ank + 1.5Dol + 0.12Gt + 2.5H_2O \quad (17)$$

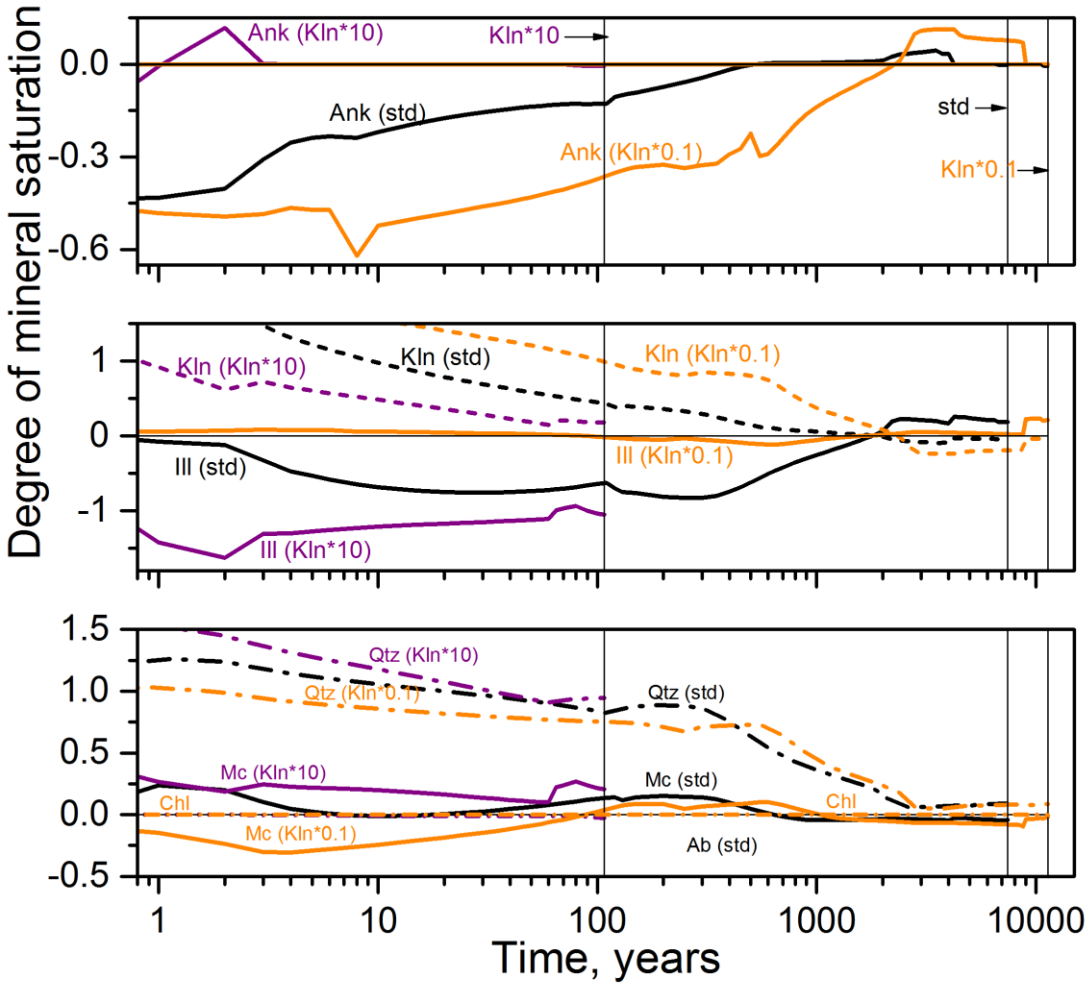

Figure 8. The time evolution of mineral saturation states in the shale at the sandstone/ shale interface for different values of the kaolinite kinetic constant. The evolution of ankerite saturation is represented in the top graph for a kaolinite kinetic constant 10 times greater than the standard constant, for the standard kinetic constant, and for the kaolinite kinetic constant equal to 1/10 the standard value. A degree of mineral saturation = 0 represents equilibrium. The saturation time profiles for kaolinite (dash) and illite (solid) are plotted in the middle graph. The saturation time profiles for quartz (long dash – dot), microcline (solid), and chlorite (dash-dot) are plotted in bottom graph. The vertical lines show the termination times for different values of the kaolinite relative kinetic constant, from left to right: 107.5, 7416, and 11,370 a for relative constants of 10, 1, and 0.1, respectively.

In this case, with Kln×10, the pore fluid becomes supersaturated with respect to ankerite within the first few years of reaction. Such a rapid onset of precipitation could be very important in real-world sequestration projects. For this case, reaction (17) replaces reaction (13) because at ~ 5 a the pore interface fluid is supersaturated with respect to kaolinite and undersaturated with respect to illite (Figure 8). It is clear that kaolinite and illite are kinetically coupled with each other (Figure 8, middle). The increase of the Kln constant moves the saturation curve of this mineral to the local equilibrium line, and moves the illite saturation curve away from equilibrium. The converse is also true (Figure 8, middle). The quartz saturation curve is also influenced by the Kln constant for 100 a (Figure 8, bottom), i.e., the activity of silica in the pore fluid increases as the Kln constant increases. This increase in silica activity results from the acceleration of oligoclase/albite dissolution in the sandstone as kaolinite precipitates faster.

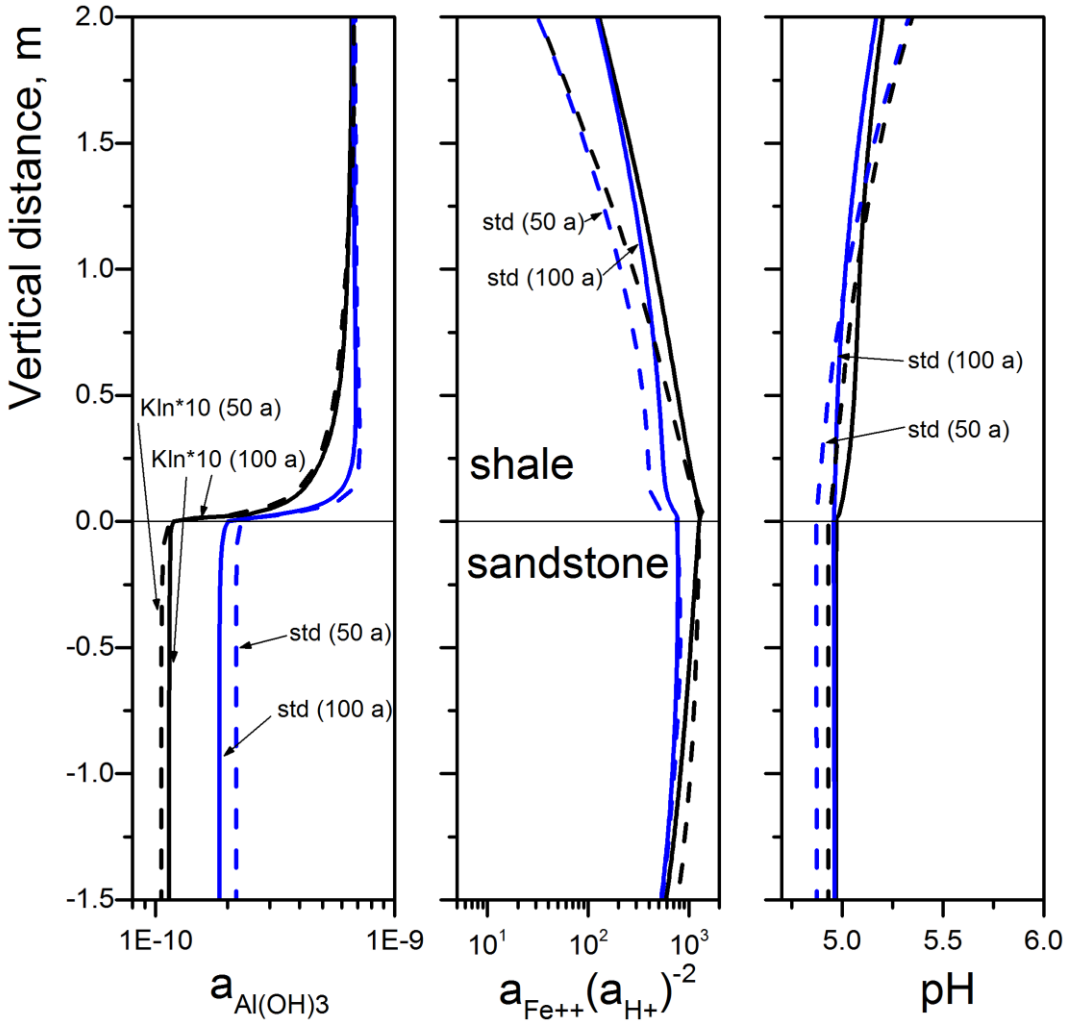

Figure 9. The activities of primary dissolved aqueous species ($a_{Al(OH)3}$ and $a_{Fe^{2+}}(a_{H^+})^{-2}$ which shows the dissolved iron thermodynamic contribution to fluid/mineral interaction) and pH

plotted versus vertical distance from the ss/sh contact (depicted at 50 and 100 a as labelled) for the case of a high value of the kaolinite kinetic constant (10 times the standard value, i.e. Kln*10) and for the standard kinetic case (std). The decrease in alumina activity in brine is accompanied by an increase in iron (II) activity in the brine.

Furthermore, because the K^+ activity is buffered by the microcline, the alumina activity in the pore fluid decreases (Figure 9, left) to balance illite dissolution and kaolinite precipitation according to reaction (9). Importantly, chlorite is always maintained very close to local chemical equilibrium with the pore fluid, and the decrease of alumina activity therefore leads to an increase in the Fe(II) activity in solution $a_{Fe^{++}}(a_{H^+})^{-2}$ (Figure 9, middle). The increase in $a_{Fe^{++}}(a_{H^+})^{-2}$ after 2 a leads to supersaturation of the fluid in ankerite, and, after 5 to 107 a, ankerite precipitates continuously (Figure 6 and 8) until porosity closure. Thus at a high kaolinite kinetic constant, reaction (17) is triggered by low alumina activity in pore solution. A similar situation is observed for Kln×3.16.

The case of a low value of the kaolinite constant (Kln×0.1) is similar to the standard simulation. Once again, an increase in the Fe(II) activity expressed as $a_{Fe^{++}}(a_{H^+})^{-2}$ occurs along with a decrease in the alumina activity and at 7000 a the solution is supersaturated by ankerite (Figure 8, top).

The simulations highlight the importance of the value of the Kln kinetic constant as well as the ferrous iron pore fluid activity. Variations in the Kln constant lead to variations in alumina – silica activities in the shale pore solution at the ss/sh interface. When chlorite is at local equilibrium with the pore solution, these activity variations change the Fe(II) activity $a_{Fe^{++}}(a_{H^+})^{-2}$, which in turn influence the ankerite degree of saturation. The beginning of ankerite precipitation triggers carbonation reactions (13) and (17).

9.2.2 ***Illite kinetic constant***

The effects of variations in the illite kinetic constant are most important in influencing the time of porosity closure. For example, the termination time at (Ill×10) equals 744.5 a, and at (Ill×0.1) equals 18990 a. Additionally, CO_2 accumulation at 7416 a for (Ill×0.1) is 30% lower than the standard simulation because less CO_2 mineral trapping occurs in this case.

However, in this case porosity at the ss/sh interface is not sealed by carbonate but rather by Kln precipitation: a high illite constant promotes intense kaolinite precipitation in the shale at the interface (Figure 10, middle). This kaolinite precipitation is accompanied by calcite precipitation (Figure 10, top), microcline precipitation (Figure 10, middle), dolomite precipitation (Figure 10, top), and strong illite dissolution (Figure 10, bottom). Overall, the reactive process is described by reaction (12) in the direction of Kln formation. In this case, the pore solution is undersaturated with respect to ankerite (Figure 10, top).

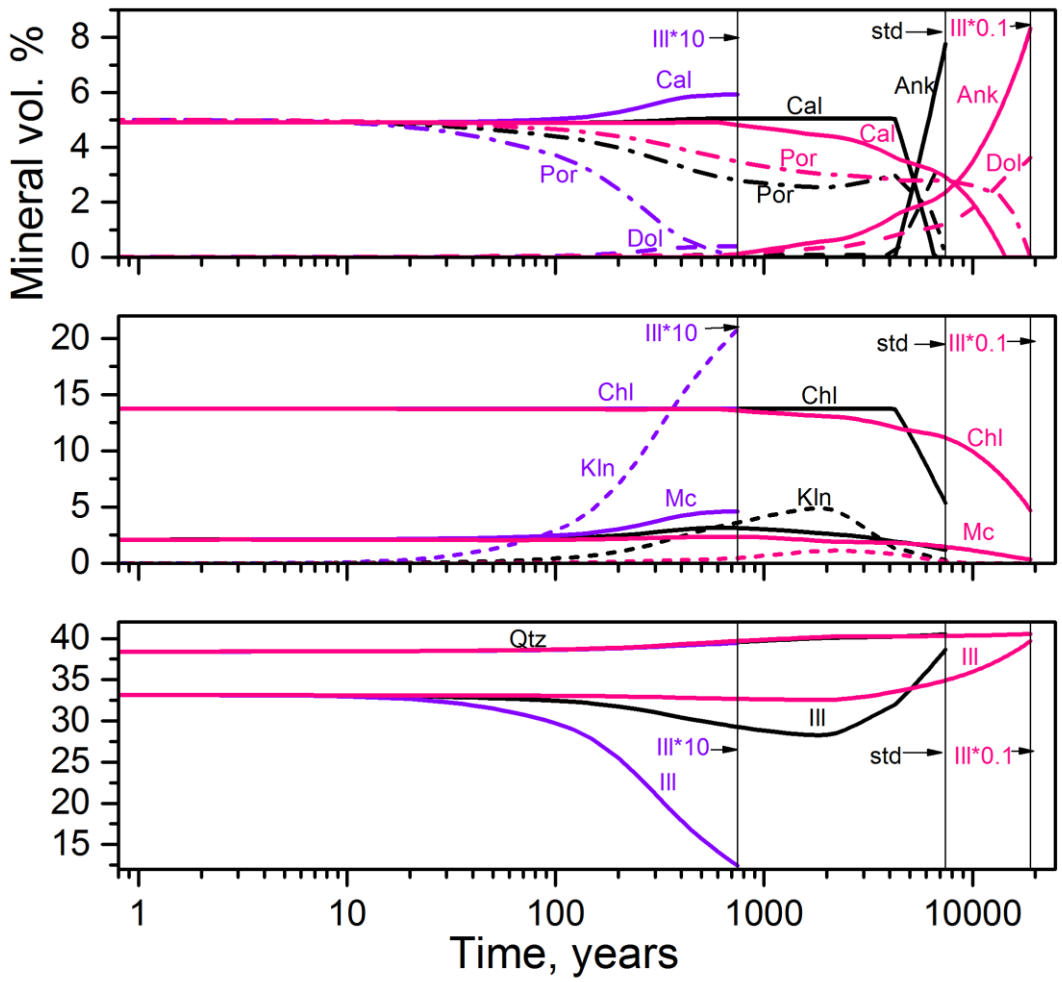

Figure 10. Plots showing the time evolution of the mineral volume fraction in the shale at the sandstone / shale interface as a function of variations in the illite kinetic constant. Top graph shows the calcite precipitation/ dissolution (solid line) and the ankerite (solid) and dolomite (dash) precipitation for a illite kinetic constant which is 10 times greater than the standard constant, the standard kinetic constant (std), and the illite kinetic constant 1/10 the standard one. The porosity evolution also is shown (dot dashed lines). The middle graph shows the chlorite dissolution (solid), kaolinite precipitation followed by dissolution (dash), and microcline precipitation/ dissolution (solid). The bottom graph depicts quartz precipitation and illite dissolution/ precipitation (solid). The vertical lines show the termination times for different values of the illite kinetic constant, from left to right: 744.5, 7416, and 18,990 a for illite relative kinetic constant values = 10, 1, and 0.1, respectively.

For a high illite kinetic constant (Ill×10), the illite saturation approaches local equilibrium and, simultaneously, the Kln saturation moves away from equilibrium. As kaolinite precipitates

in the case of a high Ill kinetic constant, the alumina activity in the pore solution stays high. The Fe(II) activity and pH remain close to their values calculated for the standard kinetics.

In contrast, for a low illite kinetic constant (Ill×0.1), illite deviates from the equilibrium at undersaturation while kaolinite approaches equilibrium. The alumina activity in pore solution at the interface decreases and the Fe(II) activity $a_{Fe^{++}}(a_{H^+})^{-2}$ increases, driving ankerite saturation to reach equilibrium much earlier (~180 a) than in the standard case (Figure 10, top). Ankerite precipitation begins at ~800 a and promotes onset of reaction (17) (Figure 10, top). After the Kln/Ill inversion at ~ 2000 a, this reaction (17) is replaced by reaction (13) with illite formation. Compared to the standard case, the rate of reaction is sluggish because of the low illite kinetic constant (Figure 10, bottom).

10. Implications

The reactive transport processes that occur at the interface of two rocks of different composition, porosity and permeability have great fundamental and practical applications. For example, such processes impact our understanding of diagenesis, contact metamorphism, radioactive waste disposal, weathering, and CO_2 sequestration. In this paper, we use a model to simulate how CO_2 interacts with minerals at a sandstone / shale contact at 75°C and 30 MPa. The simulation is meant to elucidate reactions when residual CO_2 fills 5 vol. % of the sandstone. In the simulation, the shale was modeled as a horizontal caprock layer of 5 m thickness overlying the sandstone reservoir. The upper shale boundary was maintained as no-flux. A moderate value of the inverse Archie factor (IAF) was used, i.e., 7×10^{-3}. Using literature values for all constants, ankerite + dolomite + illite form by ~ 3500 a while chlorite, calcite and microcline dissolve. Porosity at the interface was completely infilled by 7416 a.

By 7416 a, the sandstone reservoir is separated from the shale layer by an impermeable shale barrier. From a geoengineering point of view, this means that the sandstone reservoir with shale caprock is a very good storage reservoir for CO_2. We refer to this process as *auto-sealing* of the sandstone reservoir at the ss/sh contact. It is possible that ongoing precipitation might instead result in cracking of the caprock in a manner analogous to spheroidal weathering (Fletcher et al., 2006); however, two important arguments support auto-sealing rather than cracking of the caprock. First, porosity closure at the ss/sh interface is controlled by precipitation of carbonates (ankerite and dolomite) and clay minerals (illite (under standard kinetics) or kaolinite). Carbonates and clays are soft minerals that deform under stress by creep (Balashov and Yardley, 1998). Second, unlike spheroidal weathering, the reactions all take place under a confined stress at ~ 2 km depth.

The structural diffusivity of the shale pore space strongly influences the reactive process. A decrease in the Inverse Archie Factor to $(2 – 4)\times10^{-4}$ leads to retardation of porosity sealing and narrowing of the shale reactive zone. Our results exploring variations in parameters used in the extended version of Archie's law (7) are in correspondence with similar models (Shao et al., 2013) exploring reactions of hyper-alkaline solutions with marl.

The modeling showed that the minerals taking part in interactions at the ss/sh contact are divided into two groups. One group of minerals react at local equilibrium – carbonates, chlorite

and goethite—while a second group react in the kinetic regime – feldspars, clays and quartz. Although the rate of quartz reaction is slow, this reaction determines the constant decline of aqueous activity of silica as quartz slowly equilibrates (> 2000 a, Figure 2b). During the period up to ~ 2000 a, the shale pore solution at the ss/sh interface is supersaturated by Kln and undersaturated by Ill (Kln precipitates and Ill dissolves). With time, reactions in the sandstone drive the aqueous solution at the ss/sh contact to become alkaline, producing bicarbonate so that after 2000 a, the shale pore solution becomes supersaturated by illite, and undersaturated by kaolinite. For all the sensitivity tests, the time of this Kln/Ill inversion was always around 2000 a.

The predominant reaction pathway predicted in our simulation was chlorite carbonation reactions (13) or (17). The onset of this reaction was regulated by the start of ankerite precipitation, which in turn was influenced by activity Fe(II) in pore fluid. When carbonation started it was kinetically controlled by the rate of precipitation of illite or kaolinite. In general these results are in a good correspondence with observations from CO_2-enhanced oil recovery experiments and natural analogues (Kampman et al., 2014).

In another simulation of a CO_2-rich environment, Black and Haese (2014) discussed whether chlorite coatings on grains inhibit mineral reactivity (Lu et al., 2012) or whether chlorite accelerates alteration as it becomes replaced by carbonate (Armitage et al., 2013; Luquot et al., 2012; Watson et al., 2004). The results of our reactive modeling showed that both processes would be activated depending on the activities of alumina and silica in pore brine. In our simulations, chlorite always reacted close to local equilibrium with pore fluid; thus, high activities of alumina and silica correspond to low ferrous iron activity – i.e., pore brine became undersaturated with respect to ankerite. In this case chlorite demonstrated very inert reactive behavior. Conversely, low activities of alumina and silica led to an increase in the ferrous iron activity in the pore brine which triggered chlorite carbonation (13-14). This highlights the importance of the ferrous iron activity in the brine during reaction progress.

Sensitivity analyses of variations in the kinetic rate constants show that the reactive process at the ss/sh contact is most sensitive to variations in constants of kaolinite and illite, and to a lesser degree, of microcline. At high values for the kaolinite kinetic constant (Kln×10), the sandstone autoseals at the ss/sh contact at 107 a because chlorite carbonates according to reaction (17). A high illite kinetic constant (Ill×10) produces auto-sealing at 740 a due to intensive kaolinite precipitation (reaction (12)). Kln and Ill are kinetically coupled. As one of these minerals dissolves faster, the other one precipitates faster. The first mineral approaches equilibrium, in turn moving the other mineral further from equilibrium.

It is likely that the overall pattern where some minerals remain near local equilibrium (e.g. carbonates) while others react at relatively slow, kinetically-controlled rates, might be common in reactive transport in natural systems. Just like the observation that reactive transport calculations can be made faster by the assumption that some aqueous species maintain thermodynamic equilibrium at all times, multimineral CO_2 reactive transport problems could most likely be explored efficiently by assuming that some minerals (carbonates, chlorite, goethite) are maintained at equilibrium (no kinetic reactions need be incorporated into the model) while others (feldspar, clays, other aluminosilicates) remain under kinetic control. The calculations for such models would be faster than the modelling described herein.

11. Conclusions

A reactive diffusion model was used to understand the reactive transport of CO_2 in a subsurface sandstone reservoir capped by a chlorite- and illite-containing shale. The simulation focuses on the sandstone/shale (ss/sh) interface to determine the sealing properties of the shale. The calculations were carried out at 348.15 K and 30 MPa up to 20,000 a. Under standard kinetic constants during the first 2000 a, chemical reactions mostly occurred in the sandstone. From 2000 to 4000 a, Mg-Fe chlorite began being replaced by ankerite, dolomite and illite at the sandstone /shale interface. From 4000 to 7500 a, this carbonation occluded the porosity at the interface, sealing the reservoir and terminating further reaction. The potential for porosity occlusion was regulated by the amount of chlorite in the shale because this mineral provides the Mg and Fe for carbonate formation. The initial content of chlorite in the shale (assumed to have 5% initial porosity) should be greater than 8.4 vol.% to occlude porosity at the interface. However, the time sequence described above is strongly dependent on the kinetics of clay minerals. For example, an increase in the kaolinite kinetic constant by 0.5 logarithmic units hastened porosity closure by 630 a.

Extrapolating from our models, we predict that shales with higher Mg, Ca, and Fe content (e.g. more chlorite or smectite) are more likely to self-seal after CO_2 injection than other shales with a lower abundance of these cations. The implications of our modelling also show that the ultimate disposition of the CO_2 can be predicted *a priori*: potential sequestration as bicarbonate is roughly equal to the molar Na and K content of the sandstone while sequestration as carbonate mineral precipitate is roughly equal to the molar Mg, Ca, and Fe content.

Acknowledgements

This effort was performed in support of the National Energy Technology Laboratory's ongoing research in Carbon Storage under RES contract DE_FE0004000 to SLB. We are grateful to Don Rimstidt and an anonymous reviewer for their useful comments and suggestions to improve the manuscript.

References

Adabi, M. H. and Rao, P., 2003. Major and Minor Elements and their Relationship to Gold Mineralization, Beaconsfield Mine, Tasmania, Australia. *Iranian Int. J. Sci* **4**, 37-56.

Archie, G. E., 1942. The electrical resistivity log as an aid in determining some reservoir characteristics. *Transactions of the American Institute of Mechanical Engineers* **146**, 54-67.

Armitage, P. J., Faulkner, D. R., and Worden, R. H., 2013. Caprock Corrosion. *Nat. Geosci.* **6**, 79-80.

Arvidson, R. S. and Lüttge, A., 2010. Mineral Dissolution Kinetics as a Function of Distance from Equilibrium - New Experimental Results. *Chemical Geology* **269**, 79-88.

Baines, S. J. and Worden, R. H., 2004. The long-term fate of CO_2 in the subsurface: natural analogues for CO_2 storage, p.59-85. In: Baines, S. J. and Worden, R. H. Eds.), *Geological Storage of Carbon Dioxide*. The Geological Society of London, London

Balashov, V. N., Guthrie, G. D., Hakala, J. A., Lopano, C. L., Rimstidt, J. D., and Brantley, S. L., 2013. Predictive modeling of CO2 sequestration in deep saline sandstone reservoirs: Impacts of geochemical kinetics. *Applied Geochemistry* **30** 41 - 56.

Balashov, V. N. and Lebedeva, M. I., 1991. Macrokinetic Model of Origin and Development of a Monomineralic Bimetasomatic Zone, Ch. 8, p.167-195. In: Perchuk, L. L. (Ed.), *Progress in Metamorphic and Magmatic Petrology, A memorial volume in honor of D.S.Korzhinskii*. Cambridge University Press, Cambridge.

Balashov, V. N. and Yardley, B. W. D., 1998. Modeling metamorphic fluid flow with reaction-compaction-permeability feedbacks. *American Journal of Science* **298**, 441-470.

Balashov, V. N. and Zaraisky, G. P., 1982. Experimental and Theoretical Investigation of Decompaction of Rocks during Heating *Outlines of Physico-Chemical Petrology, vol.10, p.69-109*. Nauka, Moscow.

Balashov, V. N., Zaraisky, G. P., Tikhomirova, V. I., and Postnova, L. E., 1983. Diffusion of Rockforming Components in Pore Solutions at 250 C and P 100 MPa. *Geochemical International* **20**, 28-40.

Benson, S. and Cook, P., 2005. Chapter 5: Undeground geological storage. IPCC Special Report on Carbon dioxide Capture and Storage, ed. by B.Metz et al., p.195-276. In: Metz, B. e. a. (Ed.), Cambridge, U.K.

Berne, P., Bachaud, P., and Fleury, M., 2010. Duiffusion Properties of Carbonated Caprocks from the Paris Basin. *Oil & Gas Science and Technology* **65**, 473-484.

Black, J. R. and Haese, R. R., 2014. Chlorite Dissolution rates under CO_2 saturated conditions from 50 to 120 °C and 120 to 200 bar CO_2. *Geochimica et Cosmochimica Acta* **125**, 225-240.

Boving, T. B. and Grathwohl, P., 2001. Tracer diffusion in sedimentary rocks: correlation to porosity and hydraulic conductivity. *Journal of Contaminant Hydrology* **53**, 85-100.

Brace, W. F., 1977. Permeability from resistivity and pore shape. *Journal of Geopysical Research* **82**, 3343-3349.

Brantley, S. L., 2008. Kinetics of Mineral Dissolution. In: Brantley, S. L., Kubicki, J. D., and White, A. F. Eds.), *Kinetics of water-rock interaction*. Springer.

Burch, T. E., Nagy, K. L., and Lasaga, A. C., 1993. Free energy dependence of albite dissolution kinetics at 80 °C and pH 8.8. *Chemical Geology* **105**, 137-162.

Cama, J., Ganor, J., Ayora, C., and Lasaga, A. C., 2000. Smectite dissolution kinetics at 80 °C and pH 8.8. *Geochimica et Cosmochimica Acta* **64**, 2701-2717.

Cochepin, B., Trotignon, L., Bildstein, O., Steefel, C. I., Lagneau, V., and Lee, J. V. d., 2008. Approaches to modelling coupled flow and reaction in a 2D cementation experiment. *Advances in Water Resources* **31**, 1540-1551.

Collins, A. G., 1975. *Geohemistry of Oilfield Waters.* Elsevier, Amsterdam.

Doughty, C., 2010. Investigation of CO2 Plume Behavior for a Large-Scale Pilot Test of Geologic Carbon Storage in a Saline Formation. *Transp. Porous Med.* **82**, 49-76.

Duan, Z. and Sun, R., 2003. An improved model calculating CO2 solubility in pure water and aqueous NaCl solutions from 273 to 533 K and from 0 to 2000 bar. *Chemical Geology* **193**, 257-271.

Ferry, J. M., Stubbs, J. E., Guan, Y., and Eiler, J. M., 2009. Ultrastep composition gradients within ankerite grains from regionally metamorphosed marls. *Geochimica et Cosmochimica Acta* **73**, A372-A372.

Fletcher, R. C., Buss, H. L., and Brantley, S. L., 2006. A spheroidal weathering model coupling porewater chemistry to soil thicknesses during steady-state denudation. *Earth and Planetary Science Letters* **244**, 444-457.

Fleury, M., Berne, P., and Bachaud, P., 2009. Diffusion of Dissolved CO2 in Caprock. *Energy Procedia* **1**, 3461-3468.

Gaus, I., Azaroual, M., and Czernichowski-Lauriol, I., 2005. Reactive transport modelling of the impact of CO_2 injection on the clayey cap rock at Sleipner (North Sea). *Chemical Geology* **217**, 319-337.

Gautier, J.-M., Oelkers, E. H., and Schott, J., 2001. Are quartz dissolution rates proportional to BET surface areas? *Geochimica et Cosmochimica Acta* **65**, 1059-1070.

Gilfillan, S. M. V., Lollar, B. S., Holland, G., Blagburn, D., Stevens, S., Schoell, M., Cassidy, M., Ding, Z., Zhou, Z., Lacrampe-Couloume, G., and Ballentine, C. J., 2009. Solubility trapping in formation water as dominant CO_2 sink in natural gas fields. *Nature* **458**, 614-618.

Hesse, M. A., Orr Jr, F. M., and Tchelepi, H. A., 2008. Gravity currents with residual trapping. *Journal of Fluid Mechanics* **611**, 35-60.

Hosterman, J. W. and Whitlow, S. I., 1983. Clay Mineralogy of Devonian Shales in the Appalachian Basin, Geological Survey Professional Paper 1298. U.S. Government Printing Office, Washington, DC.

Jacquier, P., Hainos, D., Robinet, J. C., Herbette, M., Grenut, B., Bouchet, A., and Ferry, C., 2013. The influence of mineral variability of Callovo-Oxfordian clay rocks on radionuclide transport properties. *Applied Clay Science* **83-84**, 129-136.

Jordan, A. B., Stauffer, P. H., Harp, D., Carey, J. W., and Pawar, R. J., 2015. A response surface model to predict CO2 and brine leakage along cemented wellbores. *International Journal of Greenhouse Gas Control* **33**, 27-39.

Kampman, N., Bickle, M., Wigley, M., and Dubacq, B., 2014. Fluid flow and CO_2-fluid-mineral interactions during CO_2-storage in sedimentary basins. *Chemical Geology* **369**, 22-50.

Kang, Q., Lichtner, P. C., Viswanathan, H. S., and Abdel-Fattah, A. I., 2010. Pore Scale Modeling of Reactive Transport Involved in Geologic CO_2 Sequestration. *Transp Porous Med* **82**, 197-213.

Köhler, S. J., Dufaud, F., and Oelkers, E. H., 2003. An experimental study of illite dissolution kinetics as a function of pH from 1.4 to 12.4 and temperature from 5 to 50°C. *Geochimica et Cosmochimica Acta* **67**, 3583-3594.

Lagneau, V. and Lee, J. v. d., 2010. Operator-splitting-based reactive transport models in strong feedback of porosity change: The contribution of analytical solutions for accuracy validation and estimator improvement *Journal of Contaminant Hydrology* **112**, 118-129.

Lebedeva, M. I., Vlachos, D. G., and Tsapatsis, M., 2004. Bifurcation Analysis of Liesegang Ring Pattern Formation. *Physical Review Letters* **92**, 088301-1 - 088301-4.

Li, L., Peters, C. A., and Celia, M. A., 2007. Applicability of Averaged Concentrations in Determining Geochemical Reaction Rates in Heterogeneous Porous Media. *American Journal of Science* **307**, 1146 - 1166.

Lichtner, P. C., Pabalan, R. T., and Steefel, C. I., 1998. Model Calculations of Porosity Reduction Resulting from Cement-Tuff Diffusive Interaction. In: McKinley, I. G. and McCombie, C. Eds.)*Scientific Basis for Nuclear Waste Management XXI Book Series: Materials Research Society Symposium Proceedings, v. 506, p. 709-718*.

Lowson, R. T., Brown, P. L., Comarmond, M.-C. J., and Rajaratnam, G., 2007. The Kinetics of Chlorite Dissolution. *Geochimica et Cosmochimica Acta* **71**, 1431-1447.

Lowson, R. T., Comarmond, M.-C. J., Pajaratnam, G., and Brown, P. L., 2005. The Kinetics of the Dissolution of Chlorite as a Function of pH and at 25^{o}C. *Geochimica et Cosmochimica Acta* **69**, 1687-1699.

Lu, J., Kharaka, Y. K., Thordsen, J. J., Horita, J., Karamalidis, A., Griffith, C., Hakala, J. A., Ambats, G., Cole, D. R., Phelps, T. J., Manning, M. A., Cook, P. J., and Hovorka, S. D., 2012. CO2-Rock-Brine interactions in Lower Tuscaloosa Formation *Chemical Geology* **291**, 269-277.

Luquot, L., Andreani, M., Gouze, P., and Camps, P., 2012. CO2 Percolation Experiment through Chlorite/ Zeolite-rich Sandstone (Pretty Hill Formation - Otway Basin - Australia). *Chemical Geology* **294-295**, 75-78.

Lüttge, A., Arvidson, R. S., and Fisher, C., 2013. A Stochastic Treatment of Crystal Dissolution Kinetics. *Elements* **9**, 183-188.

Marini, L., 2007. Geological Sequestration of Carbon Dioxide. *Developments in Geochemistry 11*. Elsevier, Amsterdam.

Marty, N. C. M., Cama, J., Sato, T., Chino, D., Villiéras, F., Razafitianamaharavo, A., Brendlé, J., Giffaut, E., Soler, J. M., Gaucher, E. C., and Tounassat, C., 2011. Dissolution kinetics of synthetic Na-smectite. An integrated experimental approach. *Geochimica et Cosmochimica Acta* **75**, 5849-5864.

Marty, N. C. M., Fritz, B., Clément, A., and Michau, N., 2010. Modelling the long term alteration of the engineered bentonite barrier in an underground radioactive waste repository. *Applied Clay Science* **47**, 82-90.

Marty, N. C. M., Tournassat, C., Burnol, A., Giffaut, E., and Gaucher, E. C., 2009. Influence of reaction kinetics and mesh refinement on the numerical modelling of concrete/clay interactions. *Journal of Hydrology* **364**, 58-72.

McKibben, M. A. and Barnes, H. L., 1986. Oxidation of Pyrite in Low Temperature Acid Solutions: Rate Laws and Surface Textures. *Geochimica et Cosmochimica Acta* **50**, 1509-1520.

Milliken, K., 2002. Petrography of Ankerite Cement, Grain Replacement, and Fracture Fill in Foreland Sandstones of the Central Rocky Mountains, March 10-13, *AAPG Annual Meeting*. AAPG Search and Discovery Article #90007 2002, Houston, Texas.

Na, L., Li, L., Xiyu, Q., Huidong, Y., Lijuan, W., and Shuang, Z., 2011. Genesis of authigene carbonate minerals in the Upper Cretaceous resrvoir, Honggang Anticline, Songliao Basin: Anatural analog for mineral trapping of natural CO_2 storage. *Sedimentary Geology* **237**, 166-178.

Oelkers, E. H., 2001. General kinetic description of multioxide silicate mineral and glass dissolution. *Geochimica et Cosmochimica Acta* **65**, 3703-3719.

Palandri, J. L. and Kharaka, Y. K., 2004. A compilation of rate parameters of water-mineral interaction kinetics for application to geochemical modeling. U.S. Geological Survey, Menlo Park, California.

Pearce, J. M., Holloway, S., Wacker, H., Nelis, M. K., Rochelle, C., and Bateman, K., 1996. Natural occurences as analogues for the geological disposal of carbon dioxide. *Energy Conversion and Management* **37**, 1123-1128.

Rimstidt, J. D., Brantley, S. L., and Olsen, A. A., 2012. Systematic Review of Forsterite Dissolution Rate Data. *Geochimica et Cosmochimica Acta* **99**, 159-178.

Rimstidt, J. D. and Newcomb, W. D., 1993. Measurement and Analysis of Rate Data: The Rate of Reaction of Ferric Iron with Pyrite. *Geochimica et Cosmochimica Acta* **57**, 1919-1934.

Rochelle, C. A., Czernichowski-Lauriol, I., and Milodowski, A. E., 2004. The impact of chemical reactions on CO_2 storage in geological formations: a brief review, p.87-105. In: Baines, S. J. and Worden, R. H. Eds.), *Geological Storage of Carbon Dioxide*. Geological Society of London, London.

Sathaye, K., Hesse, M., Cassidy, M., and Stockli, D., 2014. Constraints on the Magnitude and Rate of CO2 Dissolution at Bravo Dome Natural Gas Field. *PNAS* **in press**.

Schott, J., Pokrovsky, O. S., and Oelkers, E. H., 2009. The link between mineral dissolution/precipitation kinetics and solution chemistry, Ch. 6, p. 207-258. In: Oelkers, E. H. and Schott, J. Eds.), *Themodynamics and kinetics of water-rock interaction, Reviews in Mineralogy and Geochemistry, v.70*. The Mineralogical Society of America.

Shao, H., Kosakowski, G., Berner, U., Kulik, D. A., Mäder, U., and Kolditz, O., 2013. Reactive transport modeling of the clogging process at Maqarin natural analogue site. *Physics and Chemistry of the Earth* **64**, 21-31.

Shindo, Y., Fujioka, Y., Takeuchi, K., and Komiyama, H., 1995. Kinetics on the Dissolution of CO_2 into Water from the Surface of CO_2 Hydrate at High Pressure. *International Journal of Chemical Kinetics* **27**, 569-575.

Steefel, C. I. and Lichtner, P. C., 1994. Diffusion and Reaction in Rock Matrix Bordering a Hyperalkaline Fluid-Filled Fracture. *Geochimica et Cosmochimica Acta* **58**, 3595-3612.

Steefel, C. I. and Lichtner, P. C., 1998. Multicomponent reactive transport in discrete fractures II: Infiltration of hyperalkaline groundwater at Maqarin, Jordan, a natural analogue site. *Journal of Hydrology* **209**, 200-224.

Steefel, C. I. and VanCappellen, P., 1990. A New Kinetic Approach to Modeling Water-Rock Interaction - the Role of Nucleation, Precursors, and Ostwald Ripening. *Geochimica et Cosmochimica Acta* **54**, 2657-2677.

Szulczewski, M. L., MacMinn, C. W., Herzog, H. J., and Juanes, R., 2012. Lifetime of carbon capture and storage as a climate-change mitigation technology. *PNAS* **109**, 5185-5189.

Szulczewski, M. L., MacMinn, C. W., and Juanes, R., 2014. Theoretical analysis of how pressure buildup and CO2 migration can both constrain storage capacity in deep saline aquifers. *International Journal of Greenhouse Gas Control* **23**, 113-118.

Ullman, W. J. and Aller, R. C., 1982. Diffusion coefficients in nearshore marine sediments. *Limnol. Oceanogr.* **27**, 552-556.

Van Loon, L. R., Soler, J. M., Jakob, A., and Bradbury, M. H., 2003. Effect of confining pressure on the diffusion of HTO, $^{36}Cl^-$ and $^{125}I^-$ in a layered argillaceous rock (Opallinus Clay): diffusion perpendicular to the fabric. *Applied Geochemistry* **18**, 1653-1662.

Washton, N. M., Brantley, S. L., and Mueller, K. T., 2008. Probing the molecular-level control of aluminosilicate dissolution: A sensitive solid-state NMR proxy for reactive surface area. *Geochimica et Cosmochimica Acta* **72**, 5949-5961.

Watson, M., Boreham, C. J., and Tingate, P. R., 2004. Carbon Dioxide and Carbonate Cements in the Otway basin: Implications for Geological Storage of Carbon Dioxide. *APPEA J.* **44**, 703-720.

White, A. F. and Brantley, S. L., 2003. The Effect of Time on the Weathering of Silicate Minerals: Why Do weathering Rates Differ in the Laboratory and Field? *Chemical Geology* **202**, 479-506.

Williamson, M. A. and Rimstidt, J. D., 1994. The Kinetics and Electrochemical Rate-Determining Step of Aqueous Pyrite Oxidation. *Geochimica et Cosmochimica Acta* **58**, 5443-5454.

Xu, J., Fan, C., and Teng, H. H., 2012. Calcite dissolution kinetics in view of Gibbs free energy, dislocation density, and pCO_2. *Chemical Geology* **322-323**, 11-18.

Zaraisky, G. P. and Balashov, V. N., 1995. Thermal decompaction of rocks, Ch. 10, p.253-284. In: K.I.Shmulovich, B.W.D.Yardley, and G.G.Gonchar Eds.), *Fluids in Crust: Equilibrium and Transport Properties*. Chapman & Hall, London.

Zaraisky, G. P., Balashov, V. N., and Lebedeva, M. I., 1989. Macrokinetic Model of Metasomatic Zoning. *Geokhimiya*, 1386-1395.

Zaraisky, G. P., Zharikov, V. A., Stoyanovskaya, F. M., and Balashov, V. N., 1986. *Experimental Investigation of Bimetasomatic Skarn Formation*. Nauka, Moscow.

Zhang, S., Yang, L., DePaolo, D. J., and Steefel, C. I., 2015. Chemical affinity and pH effects on chlorite dissolution kinetics under geological CO_2 sequestration related conditions. *Chemical Geology* **396**, 208-217.